

Why Diffusion Models Don't Memorize: The Role of Implicit Dynamical Regularization in Training

Tony Bonnaire^{†*} ¹, Raphaël Urfin^{††} ¹, Giulio Biroli[‡] ¹, and Marc Mézard[§] ²

¹Laboratoire de Physique de l'Ecole Normale Supérieure, ENS, Université PSL, CNRS, Sorbonne Université, Université Paris Cité, F-75005 Paris, France

²Department of Computing Sciences, Bocconi University, Milano, Italy

Abstract

Diffusion models have achieved remarkable success across a wide range of generative tasks. A key challenge is understanding the mechanisms that prevent their memorization of training data and allow generalization. In this work, we investigate the role of the training dynamics in the transition from generalization to memorization. Through extensive experiments and theoretical analysis, we identify two distinct timescales: an early time τ_{gen} at which models begin to generate high-quality samples, and a later time τ_{mem} beyond which memorization emerges. Crucially, we find that τ_{mem} increases linearly with the training set size n , while τ_{gen} remains constant. This creates a growing window of training times with n where models generalize effectively, despite showing strong memorization if training continues beyond it. It is only when n becomes larger than a model-dependent threshold that overfitting disappears at infinite training times. These findings reveal a form of implicit dynamical regularization in the training dynamics, which allow to avoid memorization even in highly overparameterized settings. Our results are supported by numerical experiments with standard U-Net architectures on realistic and synthetic datasets, and by a theoretical analysis using a tractable random features model studied in the high-dimensional limit.

Keywords: Generative Models | Diffusion Models | Memorization | Random Features

1 Introduction

Diffusion Models [DMs, 37, 14, 41, 43] achieve state-of-the-art performance in a wide variety of AI tasks such as the generation of images [34], audios [52], videos [25], and scientific data [23, 29]. This class of generative models, inspired by out-of-equilibrium thermodynamics [37], corresponds to a two-stage process: the first one, called *forward*, gradually adds noise to a data, whereas the second one, called *backward*, generates new data by denoising Gaussian white noise samples. In DMs, the reverse process typically involves solving a stochastic differential equation (SDE) with a force field called *score*. However, it is also possible to define a deterministic transport through an ordinary differential equation (ODE), treating the score as a velocity field, an approach that is for instance followed in flow matching [24].

Understanding the generalization properties of score-based generative methods is a central issue in machine learning, and a particularly important question is how memorization of the training set is avoided in practice. A model without regularization achieving zero training loss only learns the empirical score, and is bound to reproduce samples of the training dataset at the end of the backward process. This memorization regime [22, 2] is empirically observed when the training set is small and disappears when it increases beyond a model-dependent threshold [16]. Understanding the mechanisms controlling this change of regimes from memorization to generalization is a central challenge for both theory and applications. Model regularization and inductive biases imposed by the network architecture were shown to play a role [17, 36], as well as a dynamical regularization due to the finiteness of the learning rate [50]. However, the regime shift described above is consistently observed even in models where all these regularization mechanisms are present. This suggests that the core mechanism behind the transition from memorization to generalization lies elsewhere. In this work, we demonstrate – first through numerical experiments, and then via the theoretical analysis of a simplified model – that this transition is driven by an implicit bias emerging in the training dynamics, which allows to avoid the memorization phase.

*tony.bonnaire@ens.fr

†raphael.urfin@ens.fr

‡giulio.biroli@ens.fr

§marc.mezard@unibocconi.it

†Both authors contributed equally to this work.

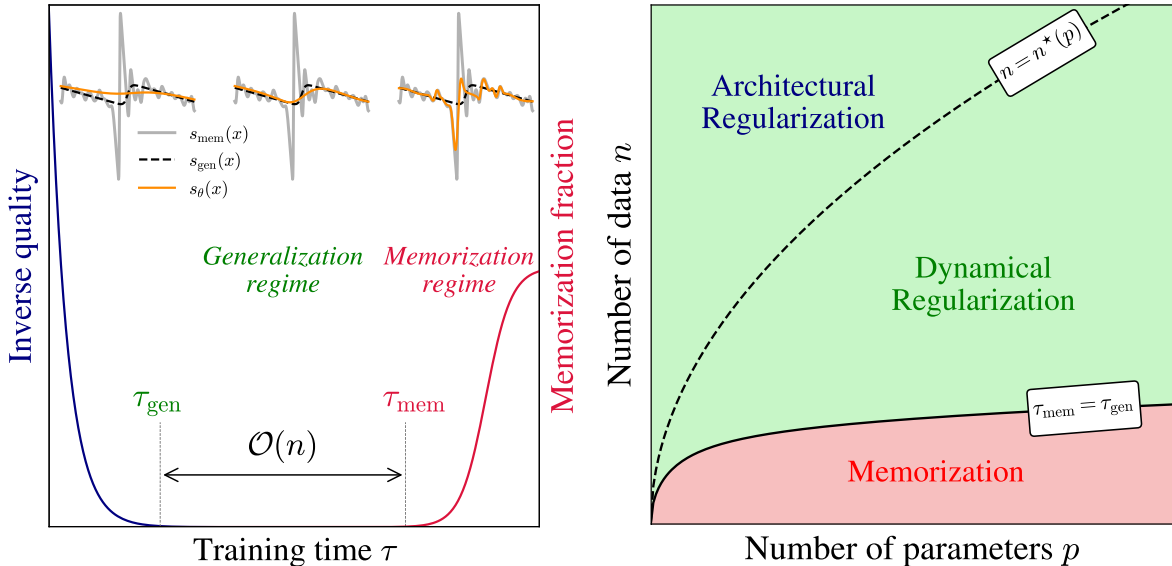


Figure 1: Qualitative summary of our contributions. (Left) Illustration of the training dynamics of a diffusion model. Depending on the training time τ , we identify three regimes measured by the inverse quality of the generated samples (blue curve) and their memorization fraction (red curve). The generalization regime extends over a large window of training times which increases with the training set size n . On top, we show a one dimensional example of the learned score function during training (orange). The gray line gives the exact empirical score, at a given noise level, while the black dashed line corresponds to the true (population) score. (Right) Phase diagram in the (n, p) plane illustrating three regimes of diffusion models: **Memorization** when n is sufficiently small at fixed p , **Architectural Regularization** for $n > n^*(p)$ (which is model and dataset dependent, as discussed in [9, 17]), and **Dynamical Regularization**, corresponding to a large intermediate generalization regime obtained when the training dynamics is stopped early, i.e. $\tau \in [\tau_{\text{gen}}, \tau_{\text{mem}}]$.

Contributions and theoretical picture. We investigate the dynamics of score learning using gradient descent, both numerically and analytically, and study the generation properties of the score depending on the time τ at which the training is stopped. The theoretical picture built from our results and combining several findings from the recent literature is illustrated in Fig. 1. The two main parameters are the size of the training set n and the expressivity of the class of score functions on which one trains the model, characterized by a number of parameters p ; when both n and p are large one can identify three main regimes. Given p , if n is larger than $n^*(p)$ (which depends on the training set and on the class of scores), the score model is not expressive enough to represent the empirical score associated to n data, and instead provides a smooth interpolation, approximately independent of the training set. In this regime, even with a very large training time $\tau \rightarrow \infty$, memorization does not occur because the model is regularized by its architecture and the finite number of parameters. When $n < n^*(p)$ the model is expressive enough to memorize, and two timescales emerge during training: one, τ_{gen} , is the minimum training time required to achieve high-quality data generation; the second, $\tau_{\text{mem}} > \tau_{\text{gen}}$, signals when further training induces memorization, and causes the model to increasingly reproduce the training samples (left panel). The first timescale, τ_{gen} , is found independent of n , whereas the second, τ_{mem} , grows approximately linearly with n , thus opening a large window of training times during which the model generalizes if early stopped when $\tau \in [\tau_{\text{gen}}, \tau_{\text{mem}}]$.

Our results shows that implicit dynamical regularization in training plays a crucial role in score-based generative models, substantially enlarging the generalization regime (see right panel of Fig. 1), and hence allowing to avoid memorization even in highly overparameterized settings. We find that the key mechanism behind the widening gap between τ_{gen} and τ_{mem} is the irregularity of the empirical score at low noise level and large n . In this regime the models used to approximate the score provide a smooth interpolation that remains stable for a long period of training times and closely approximates the population score, a behavior likely rooted in the spectral bias of neural networks [31]. Only at very long training times do the dynamics converge to the low lying minimum corresponding to the empirical score, leading to memorization (as illustrated in the one-dimensional examples in the left panel of Fig. 1).

The theoretical picture described above is based on our numerical and analytical results, and builds up on previous works, in particular numerical analysis characterizing the memorization–generalization

transition [12, 51], analytical works on memorization of DMs [9, 17, 16], and studies on the spectral bias of deep neural networks [31]. Our numerical experiments use a class of scores based on a realistic U-Net [35] trained on downsampled images of the CelebA dataset [26]. By varying n and p , we measure the evolution of the sample quality (through FID) and the fraction of memorization during learning, which support the theoretical scenario presented in Fig. 1. Additional experimental results on synthetic data are provided in Supplemental Material (SM, Sects. A and B). On the analytical side, we focus on a class of scores constructed from random features and simplified models of data, following [9]. In this setting, the timescales of training dynamics correspond directly to the inverse eigenvalues of the random feature correlation matrix. Leveraging tools from random matrix theory, we compute the spectrum in the limit of large datasets, high-dimensional data, and overparameterized models. This analysis reveals, in a fully tractable way, how the theoretical picture of Fig. 1 emerges within the random feature framework.

Related works.

- The memorization transition in DMs has been the subject of several recent empirical investigations [5, 38, 39] which have demonstrated that state-of-the-art image DMs – including Stable Diffusion and DALL·E – can reproduce a non-negligible portion of their training data, indicating a form of memorization. Several additional works [12, 51] examined how this phenomenon is influenced by factors such as data distribution, model configuration, and training procedure, and provide a strong basis for the numerical part of our work.
- A series of theoretical studies in the high-dimensional regime have analyzed the memorization–generalization transition during the generative dynamics under the empirical score assumption [2, 1, 45], showing how trajectories are attracted to the training samples. Within this high-dimensional framework, [6, 7, 48, 9] study the score learning for various model classes. In particular, [9] uses a Random Feature Neural Network [32]. The authors compute the asymptotic training and test losses for $\tau \rightarrow \infty$ and relate it to memorization. The theoretical part of our work generalizes this approach to study the role of training dynamics and early stopping in the memorization–generalization transition.
- Recent works have also uncovered complementary sources of implicit regularization explaining how DMs avoid memorization. Architectural biases and limited network capacity were for instance shown to constrain memorization in [17, 16], and finiteness of the learning rate prevents the model from learning the empirical score in [50]. Also related to our analysis, [21] provides general bounds showing the beneficial role of early stopping the training dynamics to enhance generalization for finitely supported target distributions, as well as a study of its effect for one-dimensional gaussian mixtures.
- Finally, previous studies on supervised learning [31, 53], and more recently on DMs [47], have shown that deep neural networks display a frequency-dependent learning speed, and hence a learning bias towards low frequency functions. This fact plays an important role in the results we present since the empirical score contains a low frequency part that is close to the population score, and a high-frequency part that is dataset-dependent. To the best of our knowledge, the training time to learn the high-frequency part and hence memorize, that we find to scale with n , has not been studied from this perspective in the context of score-based generative methods.

Setting: generative diffusion and score learning. Standard DMs define a transport from a target distribution P_0 in \mathbb{R}^d to a Gaussian white noise $\mathcal{N}(0, \mathbf{I}_d)$ through a *forward process* defined as an Ornstein-Uhlenbeck (OU) stochastic differential equation (SDE):

$$d\mathbf{x} = -\mathbf{x}(t)dt + d\mathbf{B}(t), \quad (1)$$

where $d\mathbf{B}(t)$ is square root of two times a Wiener process. Generation is performed by time-reversing the SDE (1) using the score function $\mathbf{s}(\mathbf{x}, t) = \nabla_{\mathbf{x}} \log P_t(\mathbf{x})$,

$$-d\mathbf{x} = [\mathbf{x}(t) + 2\mathbf{s}(\mathbf{x}, t)] dt + d\mathbf{B}(t), \quad (2)$$

where $P_t(\mathbf{x})$ is the probability density at time t along the forward process, and the noise $d\mathbf{B}(t)$ is also the square root of two times a Wiener process. As shown in the seminal works [15, 46], $\mathbf{s}(\mathbf{x}, t)$ can be

obtained by minimizing the score matching loss

$$\hat{\mathbf{s}}(\mathbf{x}, t) = \arg \min_{\mathbf{s}} \mathbb{E}_{\mathbf{x} \sim P_0, \boldsymbol{\xi} \sim \mathcal{N}(0, \mathbf{I}_d)} \left[\|\sqrt{\Delta_t} \mathbf{s}(\mathbf{x}(t), t) + \boldsymbol{\xi}\|^2 \right], \quad (3)$$

where $\Delta_t = 1 - e^{-2t}$. In practice, the optimization problem is restricted to a parametrized class of functions $\mathbf{s}_\theta(\mathbf{x}(t), t)$ defined, for example, by a neural network with parameters θ . The expectation over \mathbf{x} is replaced by the empirical average over the training set (n iid samples \mathbf{x}^ν drawn from P_0),

$$\mathcal{L}_t(\theta, \{\mathbf{x}^\nu\}_{\nu=1}^n) = \frac{1}{n} \sum_{\nu=1}^n \mathbb{E}_{\boldsymbol{\xi} \sim \mathcal{N}(0, \mathbf{I}_d)} \left[\|\sqrt{\Delta_t} \mathbf{s}_\theta(\mathbf{x}^\nu(t)) + \boldsymbol{\xi}\|^2 \right], \quad (4)$$

where $\mathbf{x}_t^\nu(\boldsymbol{\xi}) = e^{-t} \mathbf{x}^\nu + \sqrt{\Delta_t} \boldsymbol{\xi}$. The loss defined in (4) can be minimized with standard optimization tools, such as stochastic gradient descent [SGD, 33] or Adam [20]. It is also common to train only a single model conditioned on the diffusion time t with the counterpart of (4) integrated over time [18]. The solution of the minimization of (4) is the so-called empirical score (e.g. [2, 22]), defined as $\mathbf{s}_{\text{emp}}(\mathbf{x}, t) = \nabla_{\mathbf{x}} \log P_t^{\text{emp}}(\mathbf{x})$, with

$$P_t^{\text{emp}}(\mathbf{x}) = \frac{1}{n} \frac{1}{(2\pi\Delta_t)^{d/2}} \sum_{\nu=1}^n e^{-\frac{1}{2\Delta_t} \|\mathbf{x} - \mathbf{x}^\nu e^{-t}\|_2^2}. \quad (5)$$

This solution is known to inevitably recreate samples of the training set at the end of the generative process (i.e., it perfectly memorizes), unless n grows exponentially with the dimension d [2]. However, this is not the case in many practical applications where memorization is only observed for relatively small values of n , and disappears well before n becomes exponentially large in d . The empirical minimization performed in practice, within a given class of models and a given minimization procedure, does *not* drive the optimization to the global minimum of (4), but instead to a smoother estimate of the score that is independent of the training set with good generalization properties [16], as the global minimum of (3) would do. Understanding how it is possible, and in particular the role played by the training dynamics to avoid memorization is the central aim of the present work.

2 Generalization and memorization during training

Data & architecture. We conduct our experiments on the CelebA face dataset [26], which we convert to grayscale downsampled images of size $d = 32 \times 32$, and vary the training set size n from 128 up to 32768. Our score model has a U-Net architecture [35] with three resolution levels, and a base channel width of size W . All our networks are DDPMs [14] trained to predict the injected noise at diffusion time t using SGD with momentum at fixed batch size $\min(n, 512)$. The models are all conditioned on t , i.e. a single model is used to approximate the score at all times, and make use of a standard sinusoidal position embedding [44] that is added to the features of each resolution. More details about the numerical setup can be found in SM (Sect. A).

Evaluation metrics. To study the transition from generalization to memorization during training, we monitor the loss (4) at various training time τ , using a fixed diffusion time $t = 0.01$. At each τ , we compute the loss on all n training examples (training loss) and on a held-out test set of 2048 images (test loss). To characterize the score obtained after a training time τ , we assess the originality and quality of samples obtained using this score by generating 10K samples using a DDIM accelerated sampling [40]. We compute (i) the Fréchet-Inception Distance [FID, 13] against 10K test samples; and (ii) the fraction of memorized generated samples $f_{\text{mem}}(\tau)$. Following previous numerical studies [51, 12], a generated sample \mathbf{x}_τ is considered memorized if

$$\mathbb{E}_{\mathbf{x}_\tau} \left[\frac{\|\mathbf{x}_\tau - \mathbf{a}^{\mu_1}\|_2}{\|\mathbf{x}_\tau - \mathbf{a}^{\mu_2}\|_2} \right] < k, \quad (6)$$

where \mathbf{a}^{μ_1} and \mathbf{a}^{μ_2} are the nearest and second nearest neighbors of \mathbf{x}_τ in the training set in the L_2 sense. In what follows, we choose to work with $k = 1/3$ [51]. Error bars in the figures correspond to twice the standard deviation over 5 different test sets for FIDs, and 5 noise realizations for $\mathcal{L}_{\text{train}}$ and $\mathcal{L}_{\text{test}}$. For f_{mem} , we report the 95% CIs on the mean evaluated with 1,000 bootstrap samples.

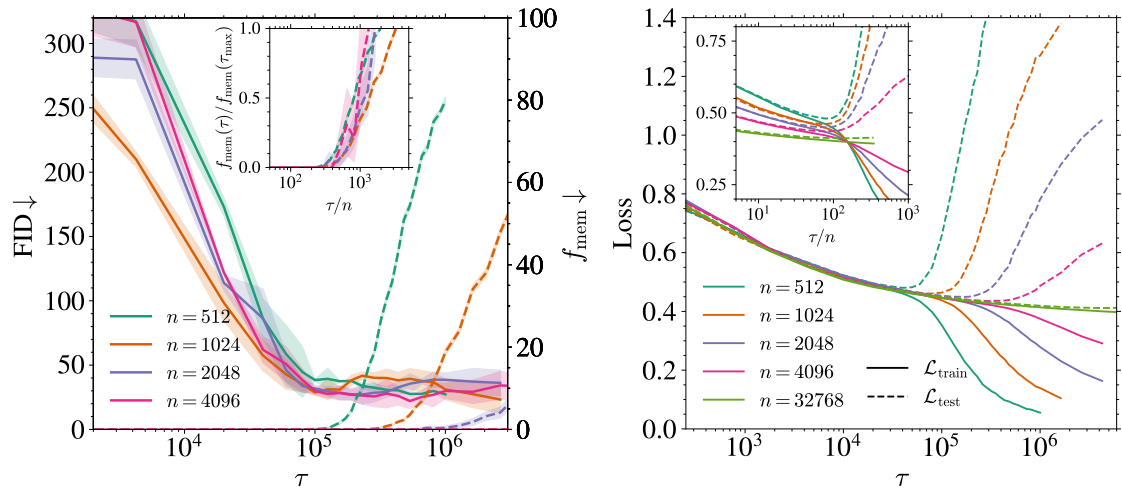


Figure 2: Memorization transition as a function of the training set size n for U-Net score models on CelebA. (Left) FID (solid lines, left axis) and memorization fraction f_{mem} (in %, dashed lines, right axis) against training time τ for various n . Inset: normalized memorization fraction $f_{\text{mem}}(\tau)/f_{\text{mem}}(\tau_{\text{max}})$ with the rescaled time τ/n . (Right) Training (solid lines) and test (dashed lines) loss with τ for several n at fixed $t = 0.01$. Inset: both losses plotted against τ/n . Error bars on the losses are imperceptible.

Role of training set size on the learning dynamics. At fixed model capacity ($p = 4 \times 10^6$, base width $W = 32$), we investigate how the training set size n impacts the previous metrics. In the left panel of Fig. 2, we first report the FID (solid lines) and $f_{\text{mem}}(\tau)$ (dashed lines) for various n . All trainings dynamics exhibit two phases. First, the FID quickly decreases to reach a minimum value on a timescale $\tau_{\text{gen}} (\approx 100\text{K})$ that does not depend on n . Beyond this time, the FID remains flat while $f_{\text{mem}}(\tau)$ remains zero until a later time τ_{mem} after which it increases, clearly signaling the entrance into a memorization regime. Both the transition time τ_{mem} and the value of the final fraction $f_{\text{mem}}(\tau_{\text{max}})$ (with τ_{max} being one to four million SGD steps) vary with n . The inset plot shows the normalized memorization fraction $f_{\text{mem}}(\tau)/f_{\text{mem}}(\tau_{\text{max}})$ against the rescaled time τ/n , making all curves collapse and increase at around $\tau/n \approx 300$, showing that $\tau_{\text{mem}} \propto n$, and demonstrating the existence of a generalization window for $\tau \in [\tau_{\text{gen}}, \tau_{\text{mem}}]$ that widens linearly with n , as illustrated in the left panel of Fig. 1.

As highlighted in the introduction, memorization in DMs is ultimately driven by the overfitting of the empirical score $\mathbf{s}_{\text{mem}}(\mathbf{x}, t)$. The evolution of $\mathcal{L}_{\text{train}}(\tau)$ and $\mathcal{L}_{\text{test}}(\tau)$ at fixed $t = 0.01$ are shown in the right panel of Fig. 2 for n ranging from 512 to 32768. Initially, the two losses remain nearly indistinguishable, indicating that the learned score $\mathbf{s}_{\theta}(\mathbf{x}, t)$ does not depend on the training set. Beyond a critical time, $\mathcal{L}_{\text{train}}$ continues to decrease while $\mathcal{L}_{\text{test}}$ increases, leading to a nonzero generalization loss whose magnitude depends on n . As n increases, this critical time also increases and, eventually, the training and test loss gap shrinks: for $n = 32768$, the test loss remains close to the training loss, even after 11 million SGD steps. The inset shows the evolution of both losses with τ/n , demonstrating that the overfitting time scales linearly with the training set size n , just like τ_{mem} identified in the left panel. Moreover, there is a consistent lag between the overfitting time and τ_{mem} at fixed n , reflecting the additional training required for the model to overfit the empirical score sufficiently to reproduce the training samples, and therefore to impact the memorization fraction.

Memorization is not due to data repetition. We must stress that this delayed memorization with n is not due to the mere repetition of training samples, as a first intuition could suggest. In SM Sects. A and B, we show that full-batch updates still yield $\tau_{\text{mem}} \propto n$. In other words, even if at fixed τ all models have processed each sample equally often, larger n consistently postpone memorization. This confirms that memorization in DMs is driven by a fundamental n -dependent change in the loss landscape – not by a sample repetition during training.

Effect of the model capacity. To study more precisely the role of the model capacity on the memorization-generalization transition, we vary the number of parameters p by changing the U-Nets base width $W \in \{16, 32, 64\}$, resulting in a total of $p \in \{1 \times 10^6, 4 \times 10^6, 16 \times 10^6\}$ parameters. In the left panel of Fig. 3, we plot both the FID (top row) and the normalized memorization fraction (bottom row) as func-

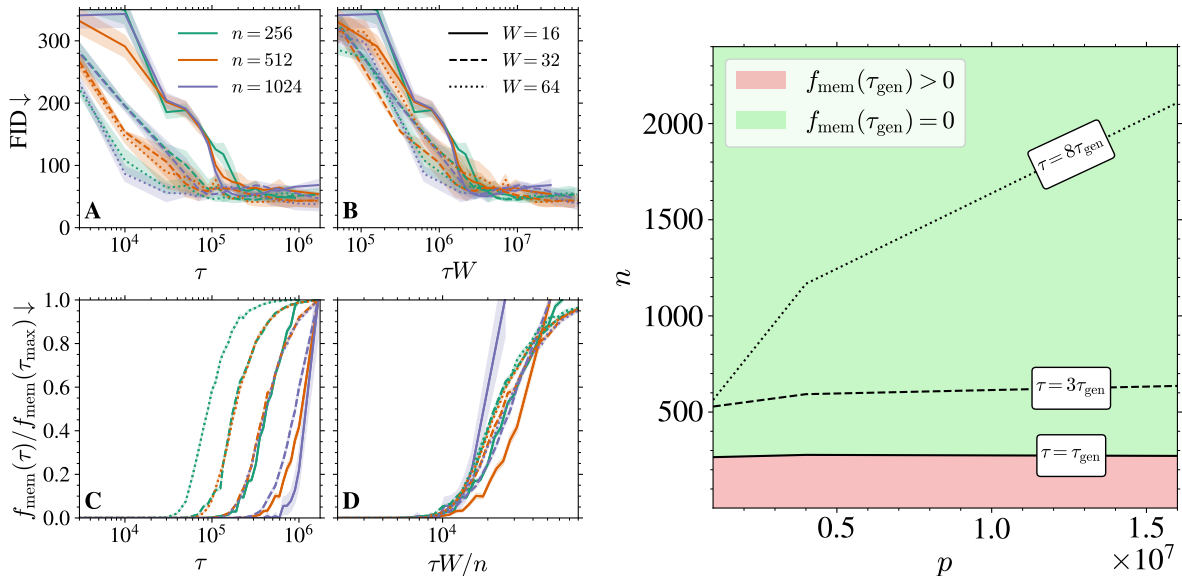


Figure 3: Effect of the number of parameters in the U-Net architecture on the timescales of the training dynamics. (Left) FID (panels A, B) and normalized memorization fraction $f_{\text{mem}}(\tau)/f_{\text{mem}}(\tau_{\text{max}})$ (panels C, D) for various n and W during training. In panels B and D, time is rescaled such that all curves collapse. (Right) (n, p) phase diagram of generalization vs memorization for U-Nets trained on CelebA. Curves show, for $\tau \in \{\tau_{\text{gen}}, 3\tau_{\text{gen}}, 8\tau_{\text{gen}}\}$, the minimal dataset size $n(p)$ satisfying $f_{\text{mem}}(\tau) = 0$. The shaded background indicates the memorization–generalization boundary for $\tau = \tau_{\text{gen}}$.

tions of τ for several width W and training set sizes n . Panels A and C demonstrate that higher-capacity networks (larger W) achieve high-quality generation and begin to memorize *earlier* than smaller ones. Panels B and D show that the two characteristic timescales simply scale as $\tau_{\text{gen}} \propto W^{-1}$ and $\tau_{\text{mem}} \propto nW^{-1}$. In particular, this implies that the critical training set size $n_{\text{gm}}(p)$ at which $\tau_{\text{mem}} = \tau_{\text{gen}}$ is approximately independent of p (at least on the limited values of p we focused on).[†] When $n > n_{\text{gm}}(p)$, the interval $[\tau_{\text{gen}}, \tau_{\text{mem}}]$ opens up, so that early stopping within this window yields high quality samples without memorization. In the right panel of Fig. 3, we display this boundary (solid line) in the (n, p) plane by fixing the training time to $\tau = \tau_{\text{gen}}$, that we identify numerically using the collapse of all FIDs at around $W\tau_{\text{gen}} \approx 3 \times 10^6$ (see panel B), and computing the smallest n such that $f_{\text{mem}}(\tau) = 0$. The resulting solid curve delineates two regimes: below the curve, memorization already starts at τ_{gen} ; above the curve, the models generalize perfectly under early stopping. We repeat this experiment for $\tau = 3\tau_{\text{gen}}$ and $\tau = 8\tau_{\text{gen}}$, obtaining successive boundaries that we expect to converge for $\tau \rightarrow \infty$ to the architectural regularization threshold $n^*(p)$, i.e. the point beyond which the network avoids memorization because it is not expressive enough, as found in [9] and highlighted in the right panel of Fig. 1.

3 Training dynamics of a Random Feature Network

Notations. We use bold symbols for vectors and matrices. The L^2 norm of a vector \mathbf{x} is denoted by $\|\mathbf{x}\| = (\sum_i x_i^2)^{1/2}$. For a variance $\sigma_{\mathbf{x}}^2$, we define a noisy variance at diffusion time t as $\Gamma_t^2 = e^{-2t}\sigma_{\mathbf{x}}^2 + \Delta_t = 1 + e^{-2t}(\sigma_{\mathbf{x}}^2 - 1)$. For an activation function σ , we define

$$\mu_1(t) = \mathbb{E}_z[\sigma(\Gamma_t z)]/\Gamma_t, \quad \mu_*^2(t) = \mathbb{E}_z[\sigma^2(\Gamma_t z)] - \Gamma_t^2 \mu_1^2(t), \quad (7)$$

where the expectation is over a standard Gaussian variable $z \sim \mathcal{N}(0, 1)$. We also define the quantity $c_t = \mathbb{E}_{u,v}[\sigma(\Gamma_t u)\sigma(\Gamma_t v)]$, where u, v are standard Gaussian variables with correlation $\mathbb{E}[uv] = e^{-2t}\sigma_{\mathbf{x}}^2/\Gamma_t^2$. We introduce $v_t^2 = c_t - e^{-2t}\sigma_{\mathbf{x}}^2\mu_1^2$ and $s_t^2 = \mu_*^2(t) - v_t^2$. We write $f = \mathcal{O}(g)$ to mean that in the limit $n, p \rightarrow \infty$, there exists a constant C such that $|f| \leq C|g|$.

[†]Establishing the full p -dependence would require an extensive study on a much larger set of model sizes. We leave this study for future works.

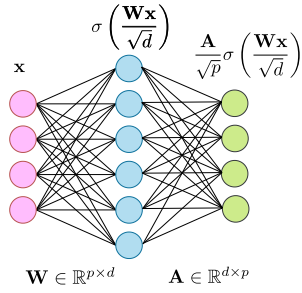


Figure 4: Illustration of an RFNN.

An RFNN, illustrated in Fig. 4, is a two-layer neural-network whose first layer weights ($\mathbf{W} \in \mathbb{R}^{p \times d}$) are drawn from a Gaussian distribution and remain frozen while the second layer weights ($\mathbf{A} \in \mathbb{R}^{d \times p}$) are learned during training, σ is a element-wise non-linear activation function. We consider a training set of n iid samples $\mathbf{x}^\nu \sim P_{\mathbf{x}} = \mathcal{N}(0, \sigma_{\mathbf{x}}^2 \mathbf{I}_d)$ for $\nu = 1, \dots, n$, and we focus on the high-dimensional limit $d, p, n \rightarrow \infty$ with the ratios $\psi_p = p/d, \psi_n = n/d$ kept fixed. We study the training dynamics associated to the minimization of the empirical score matching loss at diffusion time t defined in (4), which we rescale by a factor $1/d$ in order to ensure a finite limit at large d .

We also study the evolution of the test loss evaluated on test points and the distance to the exact score $\mathbf{s}(\mathbf{x}) = -\mathbf{x}/\Gamma_t^2$,

$$\mathcal{L}_{\text{test}} = \frac{1}{d} \mathbb{E}_{\mathbf{x}, \xi} \left[\left\| \sqrt{\Delta_t} \mathbf{s}_{\mathbf{A}}(\mathbf{x}_t(\xi)) + \xi \right\|^2 \right], \quad \mathcal{E}_{\text{score}} = \frac{1}{d} \mathbb{E}_{\mathbf{x}} \left[\left\| \mathbf{s}_{\mathbf{A}}(\mathbf{x}) + \mathbf{x}/\Gamma_t^2 \right\|^2 \right], \quad (9)$$

where the expectations $\mathbb{E}_{\mathbf{x}, \xi}$ are computed over $\mathbf{x} \sim P_{\mathbf{x}}$ and $\xi \sim \mathcal{N}(0, \mathbf{I}_d)$. The generalization loss, defined as $\mathcal{L}_{\text{gen}} = \mathcal{L}_{\text{test}} - \mathcal{L}_{\text{train}}$, indicates the degree of overfitting in the model while the distance to the exact score $\mathcal{E}_{\text{score}}$ measures the quality of the generation as it is an upper bound on the Kullback–Leibler divergence between the target and generated distributions [42, 4]. The weights \mathbf{A} are updated via gradient descent

$$\mathbf{A}^{(k+1)} = \mathbf{A}^{(k)} - \eta \nabla_{\mathbf{A}} \mathcal{L}_{\text{train}}(\mathbf{A}^{(k)}), \quad (10)$$

where η is the learning rate. In the high-dimensional limit, as the learning rate $\eta \rightarrow 0$, and after rescaling time as $\tau = k\eta/d^2$, the discrete-time dynamics converges to the following continuous-time gradient flow:

$$\dot{\mathbf{A}}(\tau) = -d^2 \nabla_{\mathbf{A}} \mathcal{L}_{\text{train}}(\mathbf{A}(\tau)) = -2\Delta_t \frac{d}{p} \mathbf{A} \mathbf{U} - \frac{2d\sqrt{\Delta_t}}{\sqrt{p}} \mathbf{V}^T, \quad (11)$$

with

$$\mathbf{U} = \frac{1}{n} \sum_{\nu=1}^n \mathbb{E}_{\xi} \left[\sigma \left(\frac{\mathbf{W} \mathbf{x}_t^\nu(\xi)}{\sqrt{d}} \right) \sigma \left(\frac{\mathbf{W} \mathbf{x}_t^\nu(\xi)}{\sqrt{d}} \right)^T \right], \quad (12)$$

$$\mathbf{V} = \frac{1}{n} \sum_{\nu=1}^n \mathbb{E}_{\xi} \left[\sigma \left(\frac{\mathbf{W} \mathbf{x}_t^\nu(\xi)}{\sqrt{d}} \right) \xi^T \right]. \quad (13)$$

To simplify the analysis, we make the two following assumptions: (i) The activation function σ admits a Hermite polynomial expansion $\sigma(x) = \sum_{s=0}^{\infty} \frac{\alpha_s}{s!} \text{Hes}(x)$ and is odd, hence $\mu_0 = \mathbb{E}_z[\sigma(z)] = 0$. In numerical applications we use $\sigma(z) = \tanh(z)$ and $\sigma_{\mathbf{x}}^2 = 1$; and (ii) The second layer \mathbf{A} is initialized with zero weights $\mathbf{A}(\tau = 0) = 0$.

Emergence of the two timescales during training. We first show in Fig. 6 that the behavior of training and test losses in the RF model mirrors the one found in realistic cases in Sect. 2, with a separation of timescales τ_{gen} and τ_{mem} which increases with n . Equation (11) is linear in \mathbf{A} and hence it can be solved exactly (see SM Sect. C). The timescales of the training dynamics are given by the inverse eigenvalues of the $p \times p$ matrix $\Delta_t \mathbf{U}/\psi_p$. Building on the Gaussian Equivalence Principle [GEP, 10, 11] and the theory of linear pencils [3], George et al. (2025) derive a coupled system of four equations characterizing the Stieltjes transform of the eigenvalue density $\rho(\lambda)$ of \mathbf{U} when $\sigma_{\mathbf{x}} = 1$. We offer an alternative derivation presented in SM for general variance using the replica method [27] – a heuristic method from the statistical physics of disordered systems – yielding the following, more compact, formulation.

Theorem 3.1. *Let $q(z) = \frac{1}{p} \text{Tr}(\mathbf{U} - z\mathbf{I})^{-1}$ and $r(z) = \frac{1}{p} \text{Tr}(\mathbf{W}^T (\mathbf{U} - z\mathbf{I})^{-1} \mathbf{W})$, with $z \in \mathbb{C}$. Then $q(z)$ and*

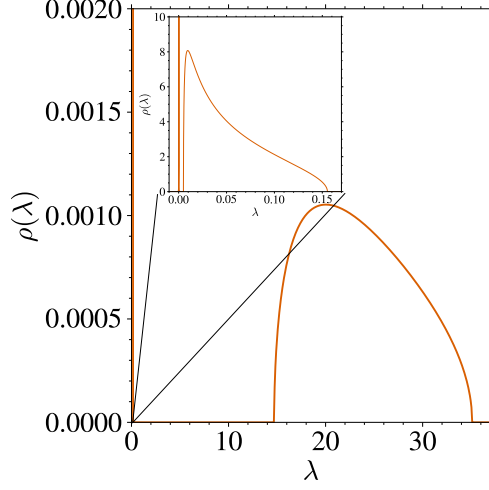


Figure 5: Spectrum of \mathbf{U} . Density $\rho(\lambda)$ computed from Theorem 3.1 with $\psi_p = 64$, $\psi_n = 32$, and $t = 0.001$. Inset: zoom on the first bulk.

$r(z)$ satisfy the following set of equations:

$$\frac{\psi_p v_t^2}{1 + \frac{e^{-2t} \mu_1^2(t) \sigma_x^2 \psi_p}{\psi_n} r + \frac{\psi_p v_t^2 q}{\psi_n}} + \psi_p (s_t^2 - z) + \frac{1 - \psi_p}{q} - \frac{r}{q^2} = 0, \quad (14)$$

$$\frac{e^{-2t} \mu_1^2(t) \sigma_x^2 \psi_p}{1 + \frac{e^{-2t} \mu_1^2(t) \sigma_x^2 \psi_p}{\psi_n} r + \frac{\psi_p v_t^2 q}{\psi_n}} + \Delta_t \mu_1^2 \psi_p + \frac{1}{q} - \frac{1}{r} = 0. \quad (15)$$

The eigenvalue distribution of \mathbf{U} , $\rho(\lambda)$, can then be obtained using the Sokhotski–Plemelj inversion formula $\rho(\lambda) = \lim_{\varepsilon \rightarrow 0^+} \frac{1}{\pi} \text{Im} q(\lambda + i\varepsilon)$.

We now focus on the asymptotic regime $\psi_p, \psi_n \gg 1$, typical for strongly over-parameterized models trained on large data sets. In this limit, the spectrum of \mathbf{U} can be described analytically by the following Theorem 3.2 (see also Fig. 5).

Theorem 3.2 (Informal). Let ρ denote the spectral density of \mathbf{U} .

Regime I: $\psi_p > \psi_n \gg 1$.

$$\rho(\lambda) = \left(1 - \frac{1 + \psi_n}{\psi_p}\right) \delta(\lambda - s_t^2) + \frac{\psi_n}{\psi_p} \rho_1(\lambda) + \frac{1}{\psi_p} \rho_2(\lambda).$$

Regime II: $\psi_n > \psi_p \gg 1$.

$$\rho(\lambda) = \left(1 - \frac{1}{\psi_p}\right) \rho_1(\lambda) + \frac{1}{\psi_p} \rho_2(\lambda).$$

Here, ρ_1 and ρ_2 are atomless measures with disjoint support. The eigenvectors associated with $\delta(\lambda - s_t^2)$ leave both training and test losses unchanged. The support of ρ_1 can be expressed as

$$\left[s_t^2 + v_t^2 (1 - \sqrt{\psi_p / \psi_n})^2, s_t^2 + v_t^2 (1 + \sqrt{\psi_p / \psi_n})^2 \right],$$

whereas ρ_2 is independent of ψ_n and its support is of order ψ_p .

The proofs of both theorems are shown in SM (Sect. C) and demonstrate the emergence of the two training timescales τ_{gen} and τ_{mem} in the RFNN model. Theorem 3.2 allows to deduce the following statements that we compare directly to the numerical results (also see SM Sect. C for a more formal version of these statements). In regime I, for $\psi_p \gg \psi_n \gg 1$, the two distinct parts of $\rho(\lambda)$, ρ_1 and ρ_2 , are well-separated, as shown in Fig. 5. This leads to two very different timescales and behaviors for the training.

Generalization: The timescale τ_{gen} on which the first relaxation takes place is associated to the formation of the generalization regime. On this timescale, which is of order one, both the training $\mathcal{L}_{\text{train}}$ and test

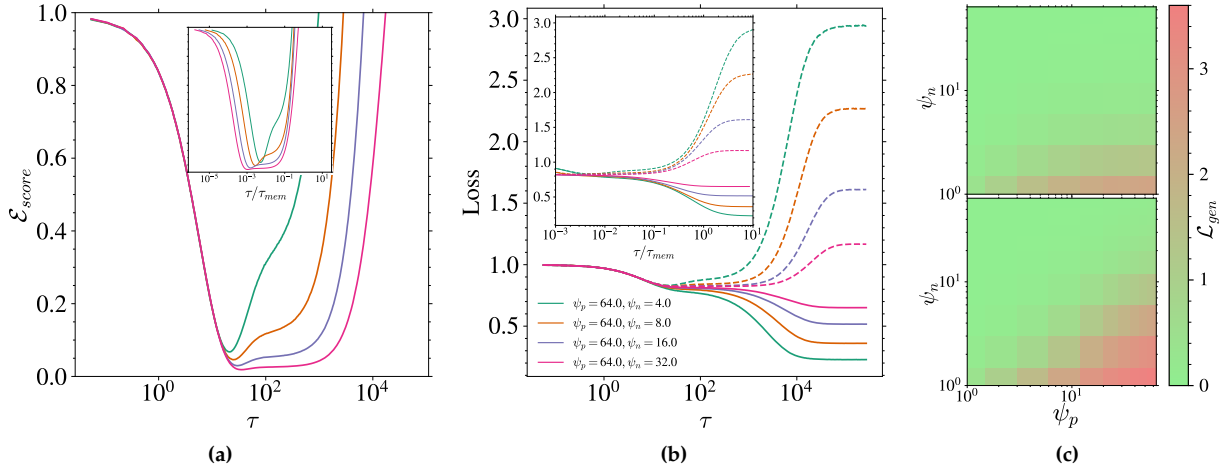


Figure 6: Evolution of the training and test losses for the RFNN. (A) Distance to the true score $\mathcal{E}_{\text{score}}$ against training time τ for $\psi_n = 4, 8, 16, 32, \psi_p = 64, t = 0.1$ and $d = 100$. The inset shows the same quantities with the training time rescaled by $\tau_{\text{mem}} = \psi_p/\Delta_t\lambda_{\text{min}}$. (B) Training (solid lines) and test (dashed lines) loss for several values of ψ_n . The inset shows both losses rescaled by τ_{mem} . (C) Colormaps of the generalization loss \mathcal{L}_{gen} for $\tau = 10^3$ (top) and $\tau = 10^4$ (bottom) as a function of ψ_n and ψ_p .

loss $\mathcal{L}_{\text{test}}$ decrease. The generalization loss $\mathcal{L}_{\text{test}} - \mathcal{L}_{\text{train}}$ is zero, and $\mathcal{E}_{\text{score}}$ tends to a value that we find to scale as $\mathcal{O}(1/\sqrt{\psi_n})$ numerically. See Fig. 6.

Memorization: The timescale τ_{mem} , on which the second stage of the dynamics takes place, is associated to overfitting and memorization. It is related to the bulk ρ_1 , and scales as $\psi_p/\Delta_t\lambda_{\text{min}}$, where λ_{min} is the left edge of ρ_1 . In the overparameterized regime $p \gg n$, τ_{mem} becomes large and $\mathcal{O}(n)$. On this timescale, the training loss decreases while the test loss increases, converging to their respective asymptotic values as computed in [9]. Fig. 6 indeed shows that all training and test curves separate, correspondingly the generalization loss \mathcal{L}_{gen} increases, at a time that scales with $\psi_p/\Delta_t\lambda_{\text{min}}$, as shown in the inset.

As n increases, the asymptotic ($\tau \rightarrow \infty$) generalization loss \mathcal{L}_{gen} decreases, indicating a reduced overfitting. For $n > n^*(p) = p$, although some overfitting remains (i.e., $\mathcal{L}_{\text{gen}} > 0$), the value of \mathcal{L}_{gen} is sensibly reduced, and the model is no longer expressive enough to memorize the training data, as shown in [9]. This regime corresponds to the *Architectural Regularization* phase in Fig. 1. We show in Fig. 6 (panel C) how the generalization loss \mathcal{L}_{gen} varies in the (n, p) plane depending on the time τ at which training is stopped. In agreement with the above results, we find that the generalization–memorization transition line depends on τ and moves upward for larger values of τ , similarly to the numerical results exposed in Fig. 3 and the illustration in Fig. 1.

4 Conclusions

We have shown that the training dynamics of neural network-based score functions display a form of implicit regularization which allows to avoid memorization even in highly overparameterized diffusion models. Specifically, we have identified two well-separated timescales in the learning: τ_{gen} , at which models begins to generate high-quality, novel samples, and τ_{mem} , beyond which they start to memorize the training data. The gap between these timescales grows with the size of the training set, leading to a broad window where early stopped models generate novel samples of high-quality. We have demonstrated that this phenomenon happens in realistic settings, for controlled synthetic data, and in analytically tractable models. Although our analysis focuses on diffusion models, the underlying score-learning mechanism we uncover is common to all score-based generative models; we therefore expect our results to generalize to this broader class.

Limitations and future works. While we derived our results under SGD optimization, most diffusion models are trained in practice with Adam [20]. In SM Sect. B, we show on synthetic datasets that the two key timescales still arise using Adam, although with much fewer optimization steps. Studying how different optimizers shift these timescales would be valuable for practical usage.

Our numerical experiments cover a range of p between 1M and 16M. Exploring a wider range is essential to map the full (n, p) phase diagram sketched in Fig. 1 and understand the precise effect of expressivity

on dynamical regularization.

Finally, our theoretical analysis rely on well-controlled data and score models that reproduce the core effects. Extending these analytical frameworks to richer data distributions (such as Gaussian mixtures or data from the hidden manifold model) and to structured architectures would be valuable to further characterize the implicit dynamical regularization of training score-functions.

Acknowledgments

The authors thank Valentin De Bortoli for initial motivating discussions on memorisation–generalisation transitions. RU thanks Beatrice Achilli, Jérôme Garnier-Brun, Carlo Lucibello and Enrico Ventura for insightful discussions. RU is grateful to Bocconi University for its hospitality during his stay, during which part of this work was conducted. This work was performed using HPC resources from GENCI-IDRIS (Grant 2025-AD011016319). GB acknowledges support from the French government under the management of the Agence Nationale PR[AI]RIE-PSAI (ANR-23-IACL-0008). MM acknowledges the support of the PNRR-PE-AI FAIR project funded by the NextGeneration EU program.

After completing this work, we became aware that A. Favero, A. Sclocchi, and M. Wyart had also been investigating the memorization–generalization transition from a similar perspective.

References

- [1] Beatrice Achilli, Enrico Ventura, Gianluigi Silvestri, Bao Pham, Gabriel Raya, Dmitry Krotov, Carlo Lucibello, and Luca Ambrogioni. Losing dimensions: Geometric memorization in generative diffusion, 2024. URL <https://arxiv.org/abs/2410.08727>.
- [2] Giulio Biroli, Tony Bonnaire, Valentin de Bortoli, and Marc Mézard. Dynamical regimes of diffusion models. *Nature Communications*, 15(9957), 2024. doi: 10.1038/s41467-024-9957-y. URL <https://www.nature.com/articles/s41467-024-9957-y>. Open access.
- [3] Antoine P. M. Bodin. *Random Matrix Methods for High-Dimensional Machine Learning Models*. Phd thesis, École Polytechnique Fédérale de Lausanne (EPFL), Lausanne, Switzerland, 2024.
- [4] Valentin De Bortoli. Convergence of denoising diffusion models under the manifold hypothesis. *Transactions on Machine Learning Research*, 2022. ISSN 2835-8856. URL <https://openreview.net/forum?id=MhK5aXo3gB>. Expert Certification.
- [5] Nicholas Carlini, Jamie Hayes, Milad Nasr, Matthew Jagielski, Vikash Sehwal, Florian Tramèr, Borja Balle, Daphne Ippolito, and Eric Wallace. Extracting training data from diffusion models. In *Proceedings of the 32nd USENIX Conference on Security Symposium, SEC '23, USA, 2023*. USENIX Association. ISBN 978-1-939133-37-3.
- [6] Hugo Cui, Florent Krzakala, Eric Vanden-Eijnden, and Lenka Zdeborova. Analysis of learning a flow-based generative model from limited sample complexity. In *The Twelfth International Conference on Learning Representations*, 2024. URL <https://openreview.net/forum?id=ndCJeysCPe>.
- [7] Hugo Cui, Cengiz Pehlevan, and Yue M. Lu. A precise asymptotic analysis of learning diffusion models: theory and insights, 2025. URL <https://arxiv.org/abs/2501.03937>.
- [8] Stéphane D’Ascoli, Maria Refinetti, Giulio Biroli, and Florent Krzakala. Double trouble in double descent: Bias and variance(s) in the lazy regime. In Hal Daumé III and Aarti Singh, editors, *Proceedings of the 37th International Conference on Machine Learning*, volume 119 of *Proceedings of Machine Learning Research*, pages 2280–2290. PMLR, 13–18 Jul 2020. URL <https://proceedings.mlr.press/v119/d-ascoli20a.html>.
- [9] Anand Jerry George, Rodrigo Veiga, and Nicolas Macris. Denoising score matching with random features: Insights on diffusion models from precise learning curves, 2025. URL <https://arxiv.org/abs/2502.00336>.
- [10] Federica Gerace, Bruno Loureiro, Florent Krzakala, Marc Mezard, and Lenka Zdeborova. Generalisation error in learning with random features and the hidden manifold model. In Hal Daumé III and Aarti Singh, editors, *Proceedings of the 37th International Conference on Machine Learning*, volume 119 of *Proceedings of Machine Learning Research*, pages 3452–3462. PMLR, 13–18 Jul 2020. URL <https://proceedings.mlr.press/v119/gerace20a.html>.

- [11] Sebastian Goldt, Bruno Loureiro, Galen Reeves, Florent Krzakala, Marc Mézard, and Lenka Zdeborová. The gaussian equivalence of generative models for learning with shallow neural networks, 2021. URL <https://arxiv.org/abs/2006.14709>.
- [12] Xiangming Gu, Chao Du, Tianyu Pang, Chongxuan Li, Min Lin, and Ye Wang. On memorization in diffusion models, 2023.
- [13] Martin Heusel, Hubert Ramsauer, Thomas Unterthiner, Bernhard Nessler, and Sepp Hochreiter. Gans trained by a two time-scale update rule converge to a local nash equilibrium, 2017.
- [14] Jonathan Ho, Ajay Jain, and Pieter Abbeel. Denoising diffusion probabilistic models, 2020.
- [15] Aapo Hyvärinen. Estimation of non-normalized statistical models by score matching. *Journal of Machine Learning Research*, 6(24):695–709, 2005. URL <http://jmlr.org/papers/v6/hyvarinen05a.html>.
- [16] Zahra Kadkhodaie, Florentin Guth, Eero P Simoncelli, and Stéphane Mallat. Generalization in diffusion models arises from geometry-adaptive harmonic representations. In *The Twelfth International Conference on Learning Representations*, 2024. URL <https://openreview.net/forum?id=ANvmVS2Yr0>.
- [17] Mason Kamb and Surya Ganguli. An analytic theory of creativity in convolutional diffusion models, 2024.
- [18] Tero Karras, Miika Aittala, Timo Aila, and Samuli Laine. Elucidating the design space of diffusion-based generative models, 2022. URL <https://arxiv.org/abs/2206.00364>.
- [19] W. F. Kibble. An extension of a theorem of mehler’s on hermite polynomials. *Mathematical Proceedings of the Cambridge Philosophical Society*, 41(1):12–15, June 1945. ISSN 0305-0041, 1469-8064. doi: 10.1017/S0305004100022313.
- [20] Diederik P. Kingma and Jimmy Ba. Adam: A method for stochastic optimization. In Yoshua Bengio and Yann LeCun, editors, *ICLR (Poster)*, 2015.
- [21] Puheng Li, Zhong Li, Huishuai Zhang, and Jiang Bian. On the generalization properties of diffusion models, 2025. URL <https://arxiv.org/abs/2311.01797>.
- [22] Sixu Li, Shi Chen, and Qin Li. A good score does not lead to a good generative model, 2024. URL <https://arxiv.org/abs/2401.04856>.
- [23] T. Li, L. Biferale, F. Bonaccorso, and et al. Synthetic lagrangian turbulence by generative diffusion models. *Nat Mach Intell*, 6:393–403, 2024. doi: 10.1038/s42256-024-00810-0. URL <https://doi.org/10.1038/s42256-024-00810-0>.
- [24] Yaron Lipman, Ricky T. Q. Chen, Heli Ben-Hamu, Maximilian Nickel, and Matthew Le. Flow matching for generative modeling. In *The Eleventh International Conference on Learning Representations*, 2023. URL <https://openreview.net/forum?id=PqvMRDCJT9t>.
- [25] Yixin Liu, Kai Zhang, Yuan Li, Zhiling Yan, Chujie Gao, Ruoxi Chen, Zhengqing Yuan, Yue Huang, Hanchi Sun, Jianfeng Gao, Lifang He, and Lichao Sun. Sora: A review on background, technology, limitations, and opportunities of large vision models, 2024.
- [26] Ziwei Liu, Ping Luo, Xiaogang Wang, and Xiaoou Tang. Deep learning face attributes in the wild. In *Proceedings of International Conference on Computer Vision (ICCV)*, December 2015.
- [27] Marc Mézard, Giorgio Parisi, and Miguel Angel Virasoro. *Spin Glass Theory and Beyond: An Introduction to the Replica Method and Its Applications*, volume 9 of *Lecture Notes in Physics*. World Scientific Publishing Company, Singapore, 1987.
- [28] Marc Potters and Jean-Philippe Bouchaud. *A First Course in Random Matrix Theory: for Physicists, Engineers and Data Scientists*. Cambridge University Press, 2020.
- [29] I. Price, A. Sanchez-Gonzalez, F. Alet, and et al. Probabilistic weather forecasting with machine learning. *Nature*, 637:84–90, 2025. doi: 10.1038/s41586-024-08252-9. URL <https://doi.org/10.1038/s41586-024-08252-9>.

- [30] S. Péché. A note on the pennington-worah distribution. *Electronic Communications in Probability*, 24: 1–7, 2019. doi: 10.1214/19-ECP255. URL <https://doi.org/10.1214/19-ECP255>.
- [31] Nasim Rahaman, Aristide Baratin, Devansh Arpit, Felix Draxler, Min Lin, Fred Hamprecht, Yoshua Bengio, and Aaron Courville. On the spectral bias of neural networks. In *International conference on machine learning*, pages 5301–5310. PMLR, 2019.
- [32] Ali Rahimi and Benjamin Recht. Random features for large-scale kernel machines. In J. Platt, D. Koller, Y. Singer, and S. Roweis, editors, *Advances in Neural Information Processing Systems*, volume 20. Curran Associates, Inc., 2007. URL https://proceedings.neurips.cc/paper_files/paper/2007/file/013a006f03dbc5392effeb8f18fda755-Paper.pdf.
- [33] Herbert Robbins and Sutton Monro. A stochastic approximation method. *The annals of mathematical statistics*, pages 400–407, 1951.
- [34] Robin Rombach, Andreas Blattmann, Dominik Lorenz, Patrick Esser, and Björn Ommer. High-resolution image synthesis with latent diffusion models, 2021.
- [35] Olaf Ronneberger, Philipp Fischer, and Thomas Brox. U-net: Convolutional networks for biomedical image segmentation. In Nassir Navab, Joachim Hornegger, William M. Wells, and Alejandro F. Frangi, editors, *Medical Image Computing and Computer-Assisted Intervention – MICCAI 2015*, pages 234–241, Cham, 2015. Springer International Publishing.
- [36] Kulin Shah, Alkis Kalavasis, Adam R. Klivans, and Giannis Daras. Does generation require memorization? creative diffusion models using ambient diffusion, 2025.
- [37] Jascha Sohl-Dickstein, Eric Weiss, Niru Maheswaranathan, and Surya Ganguli. Deep unsupervised learning using nonequilibrium thermodynamics. In Francis Bach and David Blei, editors, *Proceedings of the 32nd International Conference on Machine Learning*, volume 37 of *Proceedings of Machine Learning Research*, pages 2256–2265, Lille, France, 07–09 Jul 2015. PMLR. URL <https://proceedings.mlr.press/v37/sohl-dickstein15.html>.
- [38] Gowthami Somepalli, Vasu Singla, Micah Goldblum, Jonas Geiping, and Tom Goldstein. Diffusion art or digital forgery? investigating data replication in diffusion models. In *Proceedings of the IEEE/CVF Conference on Computer Vision and Pattern Recognition*, 2023.
- [39] Gowthami Somepalli, Vasu Singla, Micah Goldblum, Jonas Geiping, and Tom Goldstein. Understanding and mitigating copying in diffusion models. *Advances in Neural Information Processing Systems*, 36:47783–47803, 2023.
- [40] Jiaming Song, Chenlin Meng, and Stefano Ermon. Denoising diffusion implicit models, 2022. URL <https://arxiv.org/abs/2010.02502>.
- [41] Yang Song and Stefano Ermon. Generative modeling by estimating gradients of the data distribution. In H. Wallach, H. Larochelle, A. Beygelzimer, F. d’Alché-Buc, E. Fox, and R. Garnett, editors, *Advances in Neural Information Processing Systems*, volume 32. Curran Associates, Inc., 2019. URL https://proceedings.neurips.cc/paper_files/paper/2019/file/3001ef257407d5a371a96dcd947c7d93-Paper.pdf.
- [42] Yang Song, Conor Durkan, Iain Murray, and Stefano Ermon. Maximum likelihood training of score-based diffusion models, 2021.
- [43] Yang Song, Jascha Sohl-Dickstein, Diederik P. Kingma, Abhishek Kumar, Stefano Ermon, and Ben Poole. Score-based generative modeling through stochastic differential equations, 2021.
- [44] Ashish Vaswani, Noam Shazeer, Niki Parmar, Jakob Uszkoreit, Llion Jones, Aidan N Gomez, Łukasz Kaiser, and Illia Polosukhin. Attention is all you need. In I. Guyon, U. Von Luxburg, S. Bengio, H. Wallach, R. Fergus, S. Vishwanathan, and R. Garnett, editors, *Advances in Neural Information Processing Systems*, volume 30. Curran Associates, Inc., 2017. URL https://proceedings.neurips.cc/paper_files/paper/2017/file/3f5ee243547dee91fbd053c1c4a845aa-Paper.pdf.
- [45] Enrico Ventura, Beatrice Achilli, Gianluigi Silvestri, Carlo Lucibello, and Luca Ambrogioni. Manifolds, random matrices and spectral gaps: The geometric phases of generative diffusion, 2025. URL <https://arxiv.org/abs/2410.05898>.

- [46] Pascal Vincent. A connection between score matching and denoising autoencoders. *Neural Computation*, 23(7):1661–1674, 2011. doi: 10.1162/NECO_a_00142.
- [47] Binxu Wang. An analytical theory of power law spectral bias in the learning dynamics of diffusion models, 2025. URL <https://arxiv.org/abs/2503.03206>.
- [48] Peng Wang, Huijie Zhang, Zekai Zhang, Siyi Chen, Yi Ma, and Qing Qu. Diffusion models learn low-dimensional distributions via subspace clustering, 2024. URL <https://arxiv.org/abs/2409.02426>.
- [49] Wikipedia contributors. Hermite polynomials — wikipedia, the free encyclopedia. https://en.wikipedia.org/wiki/Hermite_polynomials, 2024. Accessed: 2025-05-16.
- [50] Yu-Han Wu, Pierre Marion, Gérard Biau, and Claire Boyer. Taking a big step: Large learning rates in denoising score matching prevent memorization, 2025.
- [51] TaeHo Yoon, Joo Young Choi, Sehyun Kwon, and Ernest K. Ryu. Diffusion probabilistic models generalize when they fail to memorize. In *ICML 2023 Workshop on Structured Probabilistic Inference & Generative Modeling*, 2023. URL <https://openreview.net/forum?id=shciCbSk9h>.
- [52] Chenshuang Zhang, Chaoning Zhang, Sheng Zheng, Mengchun Zhang, Maryam Qamar, Sung-Ho Bae, and In So Kweon. A survey on audio diffusion models: Text to speech synthesis and enhancement in generative ai, 2023.
- [53] Zhi-Qin John Xu Zhi-Qin John Xu, Yaoyu Zhang Yaoyu Zhang, Tao Luo Tao Luo, Yanyang Xiao Yanyang Xiao, and Zheng Ma Zheng Ma. Frequency principle: Fourier analysis sheds light on deep neural networks. *Communications in Computational Physics*, 28(5):1746–1767, January 2020. ISSN 1815-2406. doi: 10.4208/cicp.oa-2020-0085. URL <http://dx.doi.org/10.4208/cicp.OA-2020-0085>.

Why Diffusion Models Don't Memorize: The Role of Implicit Dynamical Regularization in Training

Supplementary Material (SM)

Tony Bonnaire[†], Raphaël Urfin[†], Giulio Biroli, Marc Mézard

This supplementary material provides detailed derivations and additional experiments supporting the main text. In Sect. **A**, we give details about the numerical experiments carried out in Sect. **2** of the Main Text (MT). In Sect. **B** we provide additional numerical experiments on simplified score and data models. Sect. **C** gives formal proofs of the main theorems of Sect. **3**. Finally, Sect. **D** exposes more details on the numerical experiments of Sect. **3**.

A Numerical experiments on CelebA

A.1 Details on the numerical setup

Dataset. All numerical experiments in Sect. **2** of the MT use the CelebA face dataset [26]. We center-crop each RGB image to 32×32 pixels and convert to grayscale images in order to accelerate the training of our Diffusion Models (DMs). To precisely control the samples seen by a model, no data augmentation is applied, and we vary the training set size n in the window [128, 32768]. Examples of training samples are shown in the left-most block of Fig. **7**.

Architecture. As commonly done in DDPMs implementations [e.g., 14, 43], the network approximating the score function is a U-Net [35] made of three resolution levels, each containing two residual blocks with channel multipliers $\{1, 2, 4\}$ respectively. We apply attention to the two coarsest resolutions, and embed the diffusion time via sinusoidal position embedding [44]. The base channel width W varies from 16 to 64 depending on the experiment, resulting in a total of 1 to 16 million trainable parameters.

Time reparameterization. Compared to the framework presented in the MT, the DDPMs we train make use of a time reparameterization of the forward and backward processes with a variance schedule $\{\beta_{t'}\}_{t'=1}^T$, where T is the time horizon given as a number of steps, fixed to 1000 in our experiments. The variance is evolving linearly from $\beta_1 = 10^{-4}$ to $\beta_{1000} = 2 \times 10^{-2}$. A sample at time t' , denoted $\mathbf{x}(t')$, can be expressed from $\mathbf{x}(0)$ as the following interpolation

$$\mathbf{x}(t') = \sqrt{\bar{\alpha}(t')} \mathbf{x}(0) + \sqrt{1 - \bar{\alpha}(t')} \boldsymbol{\xi}, \quad (16)$$

where $\bar{\alpha}(t') = \prod_{s=1}^{t'} (1 - \beta_s)$, and $\boldsymbol{\xi}$ is a standard and centered Gaussian noise. This is a reparameterization of the Ornstein-Uhlenbeck process from Eq. **1** defined through time t in the MT, with

$$t = -\frac{1}{2} \log(\bar{\alpha}(t')). \quad (17)$$

Training. All DMs are trained with Stochastic Gradient Descent (SGD) at fixed learning rate $\eta = 0.01$, fixed momentum $\beta = 0.95$ and batch size $B = \min(n, 512)$. We focus on SGD to facilitate the analysis of time scaling, avoiding problems that may cause alternative adaptive optimization schemes like Adam [20]. We train each model for at least 2M SGD steps, sometimes more for large values of n displaying memorization only later. We do not employ exponential moving average or learning-rate warm-up.

Generation. To accelerate sampling while preserving FID, we employ the DDIM sampler of Song et al. (2022) which replaces the Markovian reverse SDE with a deterministic, non-Markovian update. Given a trained denoiser $\boldsymbol{\xi}_\theta(\mathbf{x}_t, t)$, we iterate for $t = T', \dots, 1$

$$\mathbf{x}_{t-1} = \sqrt{\bar{\alpha}(t-1)} \frac{\mathbf{x}_t - \sqrt{1 - \bar{\alpha}(t)} \boldsymbol{\xi}_\theta(\mathbf{x}_t, t)}{\sqrt{\bar{\alpha}(t)}} + \sqrt{1 - \bar{\alpha}(t-1)} \boldsymbol{\xi}_\theta(\mathbf{x}_t, t), \quad (18)$$

[†]Both authors contributed equally to this work.

with $T' = 200$. During training, we generate at 40 milestones a set of 10,000 samples to assess generalization and memorization. Examples of samples obtained from a model trained on $n = 1024$ samples with base width $W = 32$ are shown in the middle and right blocks from Fig. 7 for two training times, $\tau = 190\text{K}$ and $\tau = 1.62\text{M}$. At $\tau = 190\text{K}$ the model generalizes ($f_{\text{mem}} = 0\%$) and achieve a test FID of 35.1. After too much training, memorization sets in and, by $\tau = 1.62\text{M}$ steps, nearly half the generated samples reproduce training images ($f_{\text{mem}} = 47.2\%$).

Statistical evaluation. FIDs [13] are computed[†] using 10,000 generated samples and 10,000 test samples, averaged over 5 independent runs with disjoint test sets. Error bars in the MT denote twice the standard deviation. Training and test losses are estimated similarly over 5 repeated evaluation on n training samples and 2048 test samples, and give negligible confidence intervals. For the memorization fraction $f_{\text{mem}}(\tau)$, we report the standard error on the mean obtained via bootstrap resampling of the 10,000 generated samples. We also verified that the scaling in the memorization time τ_{mem} is insensitive to the choice of the threshold k used to define f_{mem} in Eq. 6 by testing larger and lower values.

Computing resources. Most trainings were performed on Nvidia H100 GPUs (80GB of memory). A typical run of 2M steps takes approximately 50 hours on two GPUs and vary with the model size (defined through its base width W). In total, we train 18 distinct models for the several n, W configurations of the MT. The longest training ($n = 32768$ and $W = 32$ in Fig. 2) ran for 11M steps. The generation of 10,000 samples over 40 training times takes around an additional hour per model on the same hardware support.

A.2 Repetition and memorization

All the experiments in the MT use a fixed batch size $B = 512$, and in Sect 2 we emphasize that the observed $\mathcal{O}(n)$ scaling of τ_{mem} cannot be explained by repetition over training samples. To validate this statement, Fig. 8 shows FID and memorization fraction curves when we train the models with full-batch updates ($B = n$) for $n \in [128, 512]$. At any fixed τ , every sample has been seen exactly τ times. Yet τ_{mem} continues to grow linearly with n , as shown in the inset. This demonstrates that larger datasets reshape the loss landscape – requiring proportionally more updates to overfit – rather than simply increasing memorization through repeated exposure of training samples.

B Generalization–memorization transition in the Gaussian Mixture Model

The aim of this section is to show our results hold for other data distributions than natural images, and alternative score model that U-Net architectures.

B.1 Settings

Data distribution. We focus on data iid sampled from a d -dimensional Gaussian Mixture Model (GMM) made of two balanced Gaussians centered on $\pm\boldsymbol{\mu}$ with unit covariance, i.e.,

$$\mathbb{P}_0 = \frac{1}{2}\mathcal{N}(\boldsymbol{\mu}, \mathbf{I}_d) + \frac{1}{2}\mathcal{N}(-\boldsymbol{\mu}, \mathbf{I}_d). \quad (19)$$

In what follows, we choose to work with $\boldsymbol{\mu} = \mathbf{1}_d$, with $\mathbf{1}_d = [1, \dots, 1]^\top \in \mathbb{R}^d$. In this controlled setup, the generalization score can be computed analytically from \mathbb{P}_0 and reads

$$\mathbf{s}_{\text{gen}}(\mathbf{x}_t, t) = \boldsymbol{\mu}e^{-t} \tanh(\mathbf{x}_t \cdot \boldsymbol{\mu}e^{-t}) - \mathbf{x}_t. \quad (20)$$

Score model. The denoise $\boldsymbol{\xi}_\theta(\mathbf{x}_t, t)$ is implemented as a lightweight residual multi-layer neural network (see Fig. 9): an input layer projecting $\mathbb{R}^d \rightarrow \mathbb{R}^W$, followed by three identical residual blocks and an output layer projecting back to \mathbb{R}^d . Each block consists of two fully connected layers of width W , a skip connection, and a layer normalization. We encode the diffusion time t via sinusoidal position embedding and add it to the first feature of each block. The total number of parameter in the network

[†]Using the `pytorch-fid` Python package.



Figure 7: Training and generation on CelebA. The left-most block shows random training images. Middle and right blocks show generated samples in the left column (after $\tau = 190\text{K}$ and $\tau = 1.62\text{M}$ SGD updates respectively), alongside each sample’s nearest neighbor in the training set in the right column. All generated images come from a U-Net score model trained on $n = 1024$ CelebA images with base width $W = 32$.

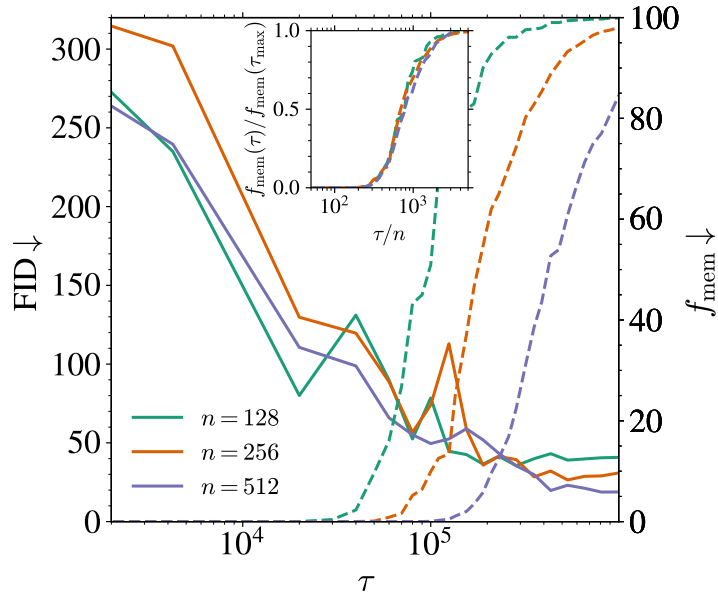


Figure 8: Memorization in CelebA with $B = n$. FID (solid lines, left axis) and memorization fraction f_{mem} (in %, dashed lines, right axis) against training time τ for various n . Inset: normalized memorization fraction $f_{\text{mem}}(\tau)/f_{\text{mem}}(\tau_{\text{max}})$ with the rescaled time τ/n .

is $p(d, W) = W(2d + 13) + d + 6W^2$. For $d = 8$, and $W = 128$, the reference setting of this section, this yields $p = 102,024$ trainable parameters.

Training and computing resources. Unless otherwise specified, we train every model of this section with SGD at fixed learning rate $\eta = 6 \times 10^{-3}$ and momentum $\beta = 0.95$ using full-batch updates $B = n$ for $n \in \{128, 256, 512, 1024, 2048, 4096\}$, running for up to 4M updates. All experiments are executed on an Nvidia RTX 2080 Ti, with the largest $n = 4096$ requiring around 10 hours to complete.

Generalization and memorization metrics. In addition to the memorization fraction $f_{\text{mem}}(\tau)$, we exploit this controlled setting where we know the true data distribution \mathbb{P}_0 to directly measure how closely it matches the generated distribution \mathbb{P}_θ via the Kullback-Leibler (KL) divergence

$$D_{\text{KL}}(\mathbb{P}_\theta|\mathbb{P}_0) = \int dx \mathbb{P}_\theta(\mathbf{x}) \log \mathbb{P}_\theta(\mathbf{x}) - \int dx \mathbb{P}_\theta(\mathbf{x}) \log \mathbb{P}_0(\mathbf{x}). \quad (21)$$

The cross-entropy term $\mathbb{E}_{\mathbb{P}_\theta} [\log \mathbb{P}_0]$ is easy to estimate using Monte Carlo,

$$\int dx \mathbb{P}_\theta(\mathbf{x}) \log \mathbb{P}_0(\mathbf{x}) \approx \frac{1}{N} \sum_{\mu=1}^N \log \mathbb{P}_0(\tilde{\mathbf{x}}_\mu), \quad (22)$$

where $\{\tilde{\mathbf{x}}_\mu\}_{\mu=1}^N$ are $N = 10,000$ samples drawn from the model with parameters $\theta(\tau)$ at training time τ . Estimating the negative entropy term $\mathbb{E}_{\mathbb{P}_\theta} [\log \mathbb{P}_\theta]$ is more challenging, since DMs only give access to the score function $\mathbf{s}_\theta(\mathbf{x}, t) = \nabla_{\mathbf{x}} \log \mathbb{P}_\theta(\mathbf{x})$ and not the underlying probability distribution \mathbb{P}_θ . We can however employ time integration to express it as a function of the score only,

$$\mathbb{E}_{\mathbb{P}_\theta} [\log \mathbb{P}_\theta] \approx \int_0^T dt I(t) - \frac{d}{2} \log(2\pi e), \quad (23)$$

with

$$I(t) = \frac{\beta_t}{2N} \sum_{\mu=1}^N [\tilde{\mathbf{x}}_\mu \mathbf{s}_\theta(\tilde{\mathbf{x}}_\mu, t) + \mathbf{s}_\theta(\tilde{\mathbf{x}}_\mu, t)^2]. \quad (24)$$

This expression assumes that the model learns an accurate representation of the score function. It is noteworthy to mention that samples are generated using standard Euler-Maruyama discretization of the

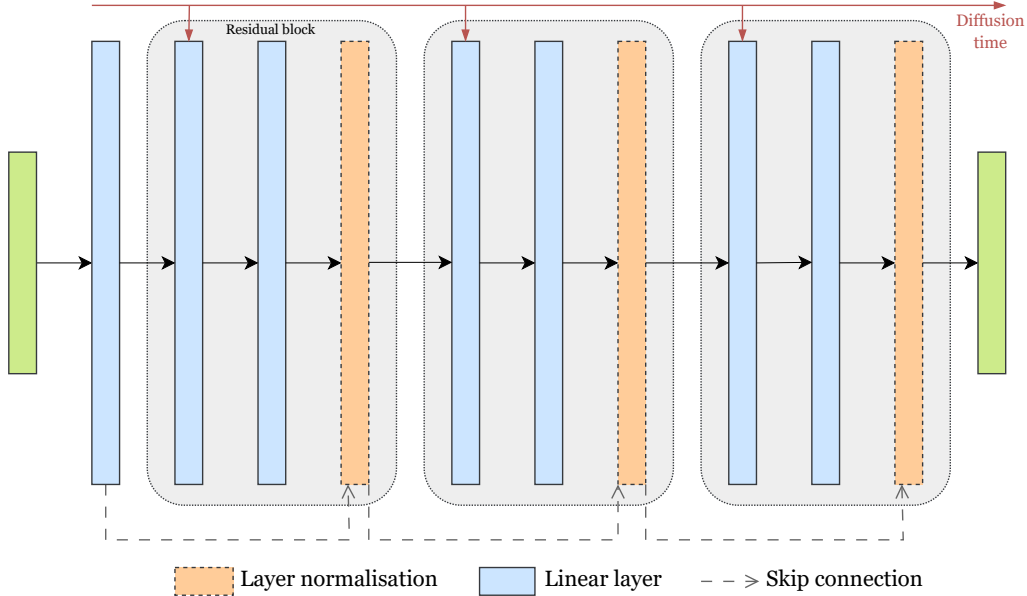


Figure 9: Basic ResNet architecture of the GMM numerical experiments. Residual network with three residual blocks, each made of two fully-connected layers followed by a layer normalization. The width of the network is W , and the input and output sizes are d .

backward process 2 of the MT over $T = 1000$ timesteps.

B.2 Scaling of τ_{mem} and τ_{gen} with n and W

In Fig. 10, the left panel shows how the KL divergence and memorization fraction evolve with training time τ for different training set sizes n at fixed width $W = 128$, while the right panel fixes $n = 2048$ and varies W . In both cases, we observe two distinct phases. First, the KL divergence decreases to near zero on a timescale τ_{gen} independent of n during which the model fully generalizes ($f_{\text{mem}} = 0$). Beyond τ_{gen} , both $D_{\text{KL}}(\mathbb{P}_\theta|\mathbb{P}_0)$ and f_{mem} begin to rise at a time τ_{mem} that scales linearly with n , as highlighted by the inset of the left panel. In contrast, both τ_{mem} scales with W^{-1} , as shown in the inset of the right panel. While the precise dependence of τ_{gen} with W remains inconclusive in this setting and require a more careful analysis, these results on the GMM mirror the main findings of the MT: the training dynamics of DMs unfolds first in a generalization phase and only later – at $\tau_{\text{mem}} \propto n/W$ – memorization begins.

B.3 What about Adam?

We conclude this section of additional experiments by repeating our analysis using the Adam optimizer [20] with learning rate $\eta = 6 \times 10^{-4}$, $(\beta_1, \beta_2) = (0.9, 0.999)$ for the gradient averages, and full-batch updates ($B = n$), keeping all other settings and evaluation metrics as above. As shown in Fig. 11, Adam yields the same two-phase training dynamics with first a generalization regime with $f_{\text{mem}} = 0$ and good performances (small D_{KL}), and later a memorization phase at $\tau_{\text{mem}} \propto n$. The only difference is that both τ_{gen} and τ_{mem} occur after much fewer steps compared to SGD. This also points out that the emergence of the two well-separated timescales and their scaling is a fundamental property of the loss landscape.

C Proofs of the analytical results

In the following we provide the mathematical arguments and the proofs for the statement in the MT. The section using the replica method is not mathematically rigorous but uses a well established method of theoretical physics, which has been already shown to provide correct results in several cases. The final

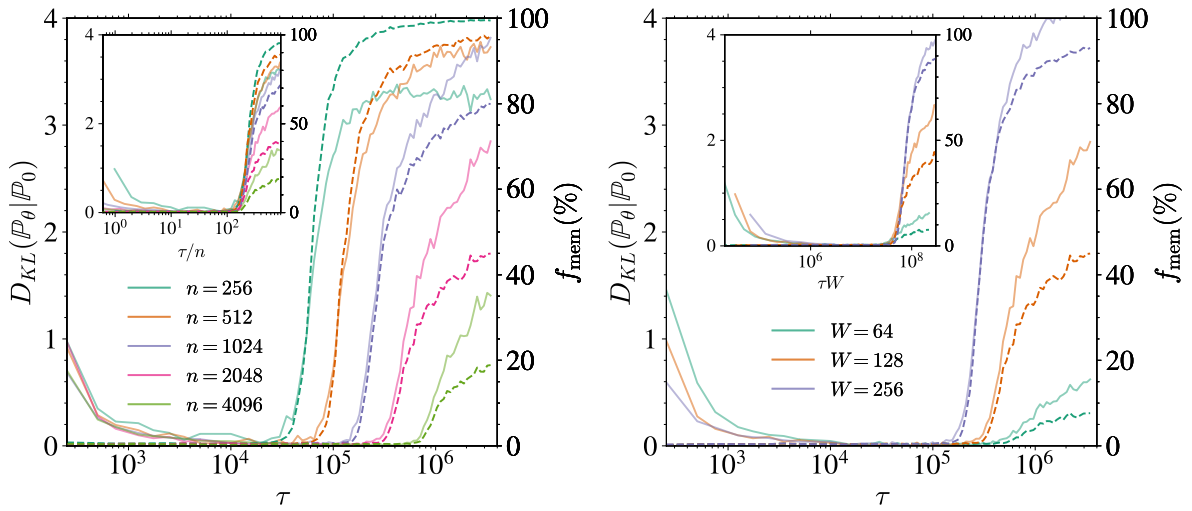


Figure 10: Generalization–Memorization transition as a function of the training set size n and width W for ResNet score models on GMM ($d = 8$). KL divergences (solid lines, left axis) and memorization fraction f_{mem} (in %, dashed lines, right axis) against training time τ for various (Left) $n \in \{256, 512, 1024, 2048, 4096\}$ at fixed $W = 128$. (Right) $W \in \{64, 128, 256\}$ at fixed $n = 2048$. Insets: $D_{\text{KL}}(\mathbb{P}_\theta|\mathbb{P}_0)$ and f_{mem} against the rescaled time τ/n (left) and τW (right).

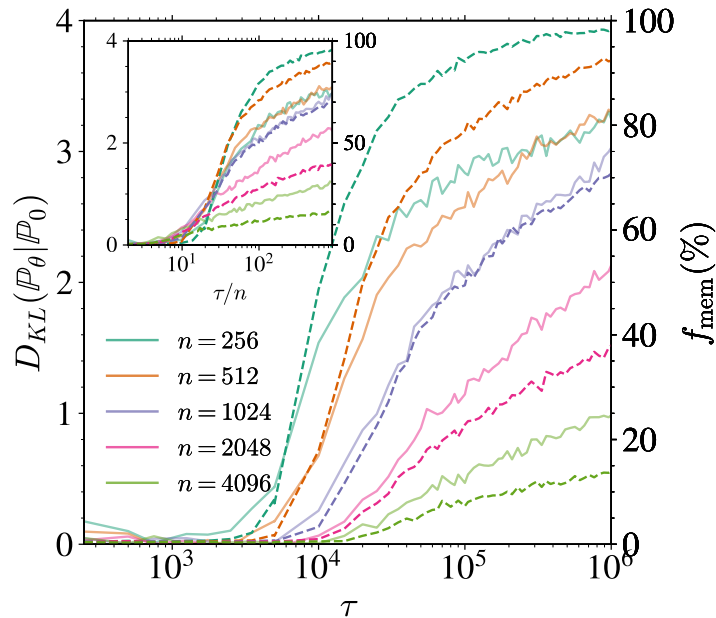


Figure 11: Generalization–Memorization transition as a function of the training set size n with Adam optimizer. KL divergences (solid lines, left axis) and memorization fraction f_{mem} (in %, dashed lines, right axis) against training time τ for various $n \in \{256, 512, 1024, 2048, 4096\}$ at fixed $W = 128$. Inset: $D_{\text{KL}}(\mathbb{P}_\theta|\mathbb{P}_0)$ and f_{mem} against the rescaled time τ/n .

result is rigorous, since it can alternatively be obtained from the rigorous free random matrix approach of [9], as shown in Sec. C.4.

C.1 Notations

We recall here the notations used throughout Sect. 3 of the MT and Sect. C of the SM.

$$d : \text{Data dimension} \quad (25)$$

$$n : \text{Numbers of data points} \quad (26)$$

$$p : \text{Dimension of the hidden layers of the RFNN} \quad (27)$$

$$\sigma(x) : \text{Activation function of the model} \quad (28)$$

$$\sigma_{\mathbf{x}}^2 = \text{Variance of the data} \quad (29)$$

$$\psi_n = \frac{n}{d} \quad (30)$$

$$\psi_p = \frac{p}{d} \quad (31)$$

$$\Gamma_t = \sqrt{\sigma_{\mathbf{x}}^2 e^{-2t} + \Delta_t} \quad (32)$$

$$\mu_1(t) = \mathbb{E}_z[\sigma(\Gamma_t z)]/\Gamma_t \quad (33)$$

$$\mu_*^2(t) = \mathbb{E}_z[\sigma^2(\Gamma_t z)] - \Gamma_t^2 \mu_1^2(t) \quad (34)$$

$$\|\sigma\|^2 = \mathbb{E}_z[\sigma(\Gamma_t z)^2] \quad (35)$$

$$\Sigma_t^2 = \begin{pmatrix} 1 & e^{-2t} \frac{\sigma_{\mathbf{x}}^2}{\Gamma_t^2} \\ e^{-2t} \frac{\sigma_{\mathbf{x}}^2}{\Gamma_t^2} & 1 \end{pmatrix} \quad (36)$$

$$c_t = \mathbb{E}_{u,v \sim \mathcal{N}(0, \Sigma_t^2)}[\sigma(\Gamma_t u)\sigma(\Gamma_t v)] \quad (37)$$

$$v_t^2 = c_t - e^{-2t} \sigma_{\mathbf{x}}^2 \mu_1^2 \quad (38)$$

$$s_t^2 = \mu_*^2 - v_t^2 \quad (39)$$

$$\mathbf{I}_d : \text{Identity matrix in dimension } d \quad (40)$$

We will denote

$$\mathbf{X} = [\mathbf{x}^1 | \dots | \mathbf{x}^n] \in \mathbb{R}^{d \times n} \quad (41)$$

the matrix whose columns are the data point vectors and likewise we decompose \mathbf{W} as

$$\mathbf{W} = [\mathbf{W}_1 | \dots | \mathbf{W}_d], \quad (42)$$

with \mathbf{W}_i the i th column of \mathbf{W} .

C.2 Closed form of the learning dynamic

Proposition C.1. *Let $\mathbf{A}(\tau)$ be the solution of the gradient flow (10) defined in the MT with initial conditions $\mathbf{A}(\tau = 0) = \mathbf{A}_0$, then*

$$\frac{\mathbf{A}(\tau)}{\sqrt{p}} = -\frac{1}{\sqrt{\Delta_t}} \mathbf{V}^T \mathbf{U}^{-1} + \left(\frac{1}{\sqrt{\Delta_t}} \mathbf{V}^T \mathbf{U}^{-1} + \frac{\mathbf{A}_0}{\sqrt{p}} \right) e^{-\frac{2\Delta_t}{\psi_p} \mathbf{U} \tau} \quad (43)$$

with

$$\mathbf{V} = \frac{1}{n} \sum_{\nu=1}^n \mathbb{E}_{\xi} \left[\sigma \left(\frac{\mathbf{W} \mathbf{x}_t^{\nu}(\xi)}{\sqrt{d}} \right) \xi^T \right]. \quad (44)$$

Proof. We expand the square in the training loss

$$\mathcal{L}_{\text{train}}(\mathbf{A}) = 1 + \frac{\Delta_t}{d} \text{Tr} \left(\frac{\mathbf{A}^T}{\sqrt{p}} \frac{\mathbf{A}}{\sqrt{p}} \mathbf{U} \right) + \frac{2\sqrt{\Delta_t}}{d} \text{Tr} \left(\frac{\mathbf{A}}{\sqrt{p}} \mathbf{V} \right) \quad (45)$$

and compute the gradient

$$\nabla_{\mathbf{A}} \mathcal{L}_{\text{train}}(\mathbf{A}(\tau)) = \frac{2\Delta_t}{d} \frac{\mathbf{A}}{p} \mathbf{U} + \frac{2\sqrt{\Delta_t}}{d\sqrt{p}} \mathbf{V}^T. \quad (46)$$

Solving this ordinary differential equation yields the desired result. Consequently, the timescales of the dynamics of $\mathbf{A}(\tau)$ is determined by the inverse of the eigenvalues of $\Delta_t \mathbf{U}/\psi_p$. \square

C.3 Gaussian Equivalence Principle

As explained in [30], the Gaussian Equivalence Theorem which applies in the high dimensional setting considered here establishes an equivalence regarding its spectral properties to a Gaussian covariate model where the nonlinear activation function is replaced by a linear term and a nonlinear term acting as noise:

$$\sigma\left(\frac{\mathbf{W}\mathbf{x}}{\sqrt{d}}\right) \rightarrow \mu_1 \frac{\mathbf{W}\mathbf{x}}{\sqrt{d}} + \mu_* \boldsymbol{\eta}, \quad \boldsymbol{\eta} \sim \mathcal{N}(0, \mathbf{I}_p), \quad (47)$$

where μ_1, μ_* are defined in Sect. C.1 for random variables \mathbf{x} drawn from $P_t = \mathcal{N}(0, \Gamma_t^2 \mathbf{I}_d)$. In this section, we outline the derivation of the Gaussian Equivalence Principle (GEP) for the matrices $\mathbf{U}, \tilde{\mathbf{U}}, \mathbf{V}$ and $\tilde{\mathbf{V}}$ under arbitrary input variance. This is a simple generalization of the result of [9], which considered only the case of data drawn from $\mathcal{N}(0, \mathbf{I}_d)$.

Lemma C.1 (Gaussian Equivalence Principle for \mathbf{U}). *In the limit $n, p, d \rightarrow \infty$ with $\psi_p = p/d, \psi_n = n/d$, the matrix*

$$\mathbf{U} = \frac{1}{n} \sum_{\nu=1}^n \mathbb{E}_{\boldsymbol{\xi}} \left[\sigma\left(\frac{\mathbf{W}\mathbf{x}_t^\nu(\boldsymbol{\xi})}{\sqrt{d}}\right) \sigma\left(\frac{\mathbf{W}\mathbf{x}_t^\nu(\boldsymbol{\xi})}{\sqrt{d}}\right)^T \right] \quad (48)$$

has the same spectrum as its GEP equivalence

$$\mathbf{U} = \frac{\mathbf{G} \mathbf{G}^T}{\sqrt{n} \sqrt{n}} + \Delta_t \mu_1^2 \frac{\mathbf{W}\mathbf{W}^T}{d} + s_t^2 \mathbf{I}_p \quad (49)$$

where

$$\mathbf{G} = e^{-t} \mu_1 \frac{\mathbf{W}}{\sqrt{d}} \mathbf{X} + v_t \boldsymbol{\Omega}, \quad (50)$$

$\mathbf{X} \in \mathbb{R}^{d \times n}$ is the matrix whose columns are the \mathbf{x}^ν s and $\boldsymbol{\Omega} \in \mathbb{R}^{p \times d}$ has gaussian entries independent of \mathbf{X} and \mathbf{W} .

Proof. For the sake of clarity, in this proof the vector \mathbf{x}^ν have variance 1 and we explicitly make the variance of the data $\sigma_{\mathbf{x}}^2$ appear. Let us focus on the element of \mathbf{U} in position (i, j)

$$\mathbf{U}_{ij} = \frac{1}{n} \sum_{\nu=1}^n \mathbb{E}_{\boldsymbol{\xi}} \left[\sigma\left(\frac{\mathbf{W}_{ik}(e^{-t} \sigma_{\mathbf{x}} \mathbf{x}_k^\nu + \sqrt{\Delta_t} \boldsymbol{\xi}_k)}{\sqrt{d}}\right) \sigma\left(\frac{\mathbf{W}_{jl}(e^{-t} \sigma_{\mathbf{x}} \mathbf{x}_l^\nu + \sqrt{\Delta_t} \boldsymbol{\xi}_l)}{\sqrt{d}}\right) \right]. \quad (51)$$

where repeated indices mean that there is a hidden sum. If $i = j$, the diagonal terms concentrate with respect to the datapoints to

$$\mathbf{U}_{ii} = \mathbb{E}_{z \sim \mathcal{N}(0,1)} [\sigma(\Gamma_t z)^2] + \mathcal{O}(1/n) = \|\sigma\|^2 + \mathcal{O}(1/n), \quad (52)$$

since the noisy data points have variance Γ_t^2 . The finite n corrections can be discarded because they cannot change the spectrum of \mathbf{U} .

Now if $i \neq j$, the expectation value on $\boldsymbol{\xi}$ can also be written as the expectation value on $u = \mathbf{W}_{ik} \boldsymbol{\xi}_k / \sqrt{d}$, $v = \mathbf{W}_{jl} \boldsymbol{\xi}_l / \sqrt{d}$ standard Gaussian random variables with correlation $\langle uv \rangle = \mathbf{W}_{ik} \mathbf{W}_{jk} / d$. Denote this expectation value as

$$\mathbb{E}_{u,v \sim P^{\mathbf{W}_{ik} \mathbf{W}_{jk}/d}} [\cdot]. \quad (53)$$

We use Mehler Kernel formula [19] to decouple u and v

$$\mathbb{E}_{u,v \sim P^\gamma}[\cdot] = \sum_{s=1}^{\infty} \frac{\gamma^s}{s!} \mathbb{E}_{u,v} [He_s(u)He_s(v)\cdot], \quad (54)$$

where now $\mathbb{E}_{u,v}[\cdot]$ is done on u and v independent and He_s are the Hermite polynomials. We remind some properties of the Hermite polynomials [49]

- They form an orthogonal base of $L^2(\mathbb{R}, \frac{e^{-x^2/2}}{\sqrt{2\pi}} dx)$.
- The first Hermite polynomials are $He_0(x) = 1, He_1(x) = x$.

Hence

$$\mathbf{U}_{ij} = \frac{1}{n} \sum_{\nu=1}^n \sum_{s=1}^{\infty} \frac{(\mathbf{W}_{ik}\mathbf{W}_{jk}/d)^s}{s!} \mathbb{E}_u [He_s(u) \sigma(\frac{\mathbf{W}_{ik}e^{-t}\sigma_{\mathbf{x}}\mathbf{x}_k^\nu}{\sqrt{d}} + \sqrt{\Delta_t}u)] \quad (55)$$

$$\times \mathbb{E}_v [He_s(v) \sigma(\frac{\mathbf{W}_{jl}e^{-t}\sigma_{\mathbf{x}}\mathbf{x}_l^\nu}{\sqrt{d}} + \sqrt{\Delta_t}v)] \quad (56)$$

$$= \frac{1}{n} \sum_{\nu=1}^n (\mathbb{E}_u [\sigma(\frac{\mathbf{W}_{ik}e^{-t}\sigma_{\mathbf{x}}\mathbf{x}_k^\nu}{\sqrt{d}} + \sqrt{\Delta_t}u)] \mathbb{E}_v [\sigma(\frac{\mathbf{W}_{jl}e^{-t}\sigma_{\mathbf{x}}\mathbf{x}_l^\nu}{\sqrt{d}} + \sqrt{\Delta_t}v)]) \quad (57)$$

$$+ \frac{1}{n} \sum_{\nu=1}^n \frac{\mathbf{W}_{ik}\mathbf{W}_{jk}}{d} \mathbb{E}_u [u \sigma(\frac{\mathbf{W}_{ik}e^{-t}\sigma_{\mathbf{x}}\mathbf{x}_k^\nu}{\sqrt{d}} + \sqrt{\Delta_t}u)] \mathbb{E}_v [v \sigma(\frac{\mathbf{W}_{jl}e^{-t}\sigma_{\mathbf{x}}\mathbf{x}_l^\nu}{\sqrt{d}} + \sqrt{\Delta_t}v)] \quad (58)$$

$$= \frac{1}{n} \sum_{\nu=1}^n (\mathbb{E}_u [\sigma(\frac{\mathbf{W}_{ik}e^{-t}\sigma_{\mathbf{x}}\mathbf{x}_k^\nu}{\sqrt{d}} + \sqrt{\Delta_t}u)] \mathbb{E}_v [\sigma(\frac{\mathbf{W}_{jl}e^{-t}\sigma_{\mathbf{x}}\mathbf{x}_l^\nu}{\sqrt{d}} + \sqrt{\Delta_t}v)] + \quad (59)$$

$$\frac{\mathbf{W}_{ik}\mathbf{W}_{jk}}{d} \mathbb{E}_{\mathbf{x}} [\mathbb{E}_u [u \sigma(\frac{\mathbf{W}_{ik}e^{-t}\sigma_{\mathbf{x}}\mathbf{x}_k^\nu}{\sqrt{d}} + \sqrt{\Delta_t}u)] \mathbb{E}_v [v \sigma(\frac{\mathbf{W}_{jl}e^{-t}\sigma_{\mathbf{x}}\mathbf{x}_l^\nu}{\sqrt{d}} + \sqrt{\Delta_t}v)]], \quad (60)$$

by neglecting order $\mathcal{O}(1/d)$ terms. Let us first focus on the second term. We expand $\sigma(\Gamma_t \cdot)$ on the Hermite polynomials base $\{He_s\}_{s \geq 0}$.

$$\sigma(\Gamma_t x) = \sum_{s=1}^{\infty} \frac{\alpha_s}{s!} He_s(x), \quad \alpha_s = \mathbb{E}_z [\sigma(\Gamma_t z) He_s(z)]. \quad (61)$$

$$\mathbb{E}_u [u \sigma(\frac{\mathbf{W}_{ik}e^{-t}\sigma_{\mathbf{x}}\mathbf{x}_k^\nu}{\sqrt{d}} + \sqrt{\Delta_t}u)] = \sum_{s=1}^{\infty} \frac{\alpha_s}{s!} \mathbb{E}_u [u He_s(\frac{1}{\Gamma_t} (\frac{\mathbf{W}_{ik}e^{-t}\sigma_{\mathbf{x}}\mathbf{x}_k^\nu}{\sqrt{d}} + \sqrt{\Delta_t}u))] \quad (62)$$

$$= \sqrt{\Delta_t} \alpha_1 / \Gamma_t, \quad (63)$$

hence the second term gives $\frac{\mathbf{W}\mathbf{W}^T}{d} \Delta_t \alpha_1^2 / \Gamma_t^2 = \frac{\mathbf{W}\mathbf{W}^T}{d} \Delta_t \mu_1^2$. For the first term

$$\frac{1}{n} \sum_{\nu=1}^n (\mathbb{E}_u [\sigma(\frac{\mathbf{W}_{ik}e^{-t}\sigma_{\mathbf{x}}\mathbf{x}_k^\nu}{\sqrt{d}} + \sqrt{\Delta_t}u)] \mathbb{E}_v [\sigma(\frac{\mathbf{W}_{jl}e^{-t}\sigma_{\mathbf{x}}\mathbf{x}_l^\nu}{\sqrt{d}} + \sqrt{\Delta_t}v)]), \quad (64)$$

we first denote $\sigma_0(x) = \mathbb{E}_z [\sigma(e^{-t}\sigma_{\mathbf{x}}x + \sqrt{\Delta_t}z)]$. It is thus equal to

$$\frac{1}{n} \sum_{\nu=1}^n \sigma_0(\frac{\mathbf{W}_{ik}\mathbf{x}_k^\nu}{\sqrt{d}}) \sigma_0(\frac{\mathbf{W}_{jl}\mathbf{x}_l^\nu}{\sqrt{d}}). \quad (65)$$

We use the GEP on σ_0 and its argument $\frac{\mathbf{W}_{ik}\mathbf{x}_k^\nu}{\sqrt{d}}$ of variance 1

$$\sigma_0(\frac{\mathbf{W}\mathbf{X}}{\sqrt{d}}) = \mathbb{E}_z [\sigma_0(z)z] \frac{\mathbf{W}\mathbf{X}}{\sqrt{d}} + \sqrt{\mathbb{E}_z [\sigma_0(z)^2] - \mathbb{E}_z [\sigma_0(z)z]^2} \mathbf{\Omega}, \quad (66)$$

$$\mathbb{E}_z [\sigma_0(z)z] = \mathbb{E}_{z,u} [\sigma(e^{-t}\sigma_{\mathbf{x}}z + \sqrt{\Delta_t}u)z] = e^{-t}\sigma_{\mathbf{x}}\mu_1 / \Gamma_t, \quad (67)$$

$$\mathbb{E}_z[\sigma_0(z)^2] = \mathbb{E}_{z,u,v}[\sigma(e^{-t}\sigma_x z + \sqrt{\Delta_t}u)\sigma(e^{-t}\sigma_x z + \sqrt{\Delta_t}v)] \quad (68)$$

$$= \mathbb{E}_{u,v \sim P^{e^{-2t}\sigma_x^2/\Gamma_t^2}}[\sigma(\Gamma_t u)\sigma(\Gamma_t v)] = c_t. \quad (69)$$

hence the zero order term can be written as

$$\frac{1}{n} \left(\frac{e^{-t}\mu_1\sigma_x}{\Gamma_t} \frac{\mathbf{W}\mathbf{X}}{\sqrt{d}} + \sqrt{c_t - e^{-2t}\sigma_x^2\mu_1^2/\Gamma_t^2} \boldsymbol{\Omega} \right) \left(\frac{e^{-t}\mu_1\sigma_x}{\Gamma_t} \frac{\mathbf{W}\mathbf{X}}{\sqrt{d}} + \sqrt{c_t - e^{-2t}\sigma_x^2\mu_1^2/\Gamma_t^2} \boldsymbol{\Omega} \right)^T. \quad (70)$$

To finish the analysis we need to take care of the diagonal term. It must be equal to $\|\sigma\|^2$. The zero order term give $c_t - e^{-2t}\mu_1^2 + e^{-t}\mu_1 = \Delta_t\mu_1^2$ while the first order gives $\Delta_t\mu_1^2$ hence we need to add a term $\|\sigma\|^2 - c_t - \Delta_t\mu_1^2 = s_t^2$. Hence the GEP of \mathbf{U} reads

$$\mathbf{U} = \frac{\mathbf{G}}{\sqrt{n}} \frac{\mathbf{G}^T}{\sqrt{n}} + \Delta_t\mu_1^2 \frac{\mathbf{W}\mathbf{W}^T}{d} + s_t^2 \mathbf{I}_p. \quad (71)$$

□

Lemma C.2 (GEP for $\tilde{\mathbf{U}}$). *Let*

$$\tilde{\mathbf{U}} = \mathbb{E}_{\mathbf{y}} \left[\sigma \left(\frac{\mathbf{W}\mathbf{y}}{\sqrt{d}} \right) \sigma \left(\frac{\mathbf{W}\mathbf{y}}{\sqrt{d}} \right)^T \right], \quad (72)$$

where the expectation value is over $\mathbf{y} \sim \mathcal{N}(0, \Gamma_t^2 \mathbf{I}_p)$. Then the GEP of $\tilde{\mathbf{U}}$ reads

$$\mu_1^2 \Gamma_t^2 \frac{\mathbf{W}\mathbf{W}^T}{d} + \mu_*^2 \mathbf{I}_p. \quad (73)$$

Proof. Replace σ by its GEP,

$$\sigma \left(\frac{\mathbf{W}\mathbf{y}}{\sqrt{d}} \right) = \mu_1 \frac{\mathbf{W}\mathbf{y}}{\sqrt{d}} + \mu_* \boldsymbol{\Omega}, \quad (74)$$

where $\boldsymbol{\Omega} \in \mathbb{R}^{p \times n}$ has gaussian entries independent of \mathbf{y} . Injecting this decomposition into the expectation value and using the fact that $\mathbf{y}\mathbf{y}^T$ and $\boldsymbol{\Omega}\boldsymbol{\Omega}^T$ have respectively mean $\Gamma_t^2 \mathbf{I}_p$ and \mathbf{I}_p one ends up with the result of the lemma. □

Lemma C.3 (GEP for \mathbf{V} and $\tilde{\mathbf{V}}$). *Let*

$$\mathbf{V} = \frac{1}{n} \sum_{\nu=1}^n \mathbb{E}_{\boldsymbol{\xi}} \left[\sigma \left(\frac{\mathbf{W}\mathbf{x}_t^\nu(\boldsymbol{\xi})}{\sqrt{d}} \right) \boldsymbol{\xi}^T \right], \quad (75)$$

$$\tilde{\mathbf{V}} = \mathbb{E}_{\mathbf{x}, \boldsymbol{\xi}} \left[\sigma \left(\frac{\mathbf{W}\mathbf{x}_t(\boldsymbol{\xi})}{\sqrt{d}} \right) \boldsymbol{\xi}^T \right]. \quad (76)$$

They can be replaced by their Gaussian Equivalence Principle in the train and test losses.

$$\tilde{\mathbf{V}} = \mathbf{V} = \mu_1 \sqrt{\Delta_t} \frac{\mathbf{W}}{\sqrt{d}}. \quad (77)$$

Proof. In this case, one can directly do the GEP on σ since the deterministic noise $\boldsymbol{\Omega}$ appears only multiplied to $\boldsymbol{\xi}$ in the expectation and thus the expectation value of this term with respect to $\boldsymbol{\xi}$ vanishes. Let us do it for $\tilde{\mathbf{V}}$ and it is the same for \mathbf{V} . One can writes

$$\sigma \left(\frac{\mathbf{W}\mathbf{x}_t(\boldsymbol{\xi})}{\sqrt{d}} \right) = \mu_1 \frac{\mathbf{W}\mathbf{x}_t(\boldsymbol{\xi})}{\sqrt{d}} + \mu_* \boldsymbol{\Omega}, \quad (78)$$

with $\boldsymbol{\Omega}$ with gaussian entries independent of $\mathbf{x}_t(\boldsymbol{\xi})$. Since $\mathbf{x}_t(\boldsymbol{\xi}) = e^{-t}\mathbf{x} + \sqrt{\Delta_t}\boldsymbol{\xi}$, one obtains

$$\tilde{\mathbf{V}} = \mu_1 \sqrt{\Delta_t} \frac{\mathbf{W}}{\sqrt{d}}. \quad (79)$$

It is easy to see that this computation also works for $\tilde{\mathbf{V}}$. □

C.4 Proof of Theorem 3.1

We recall the Theorem 3.1 of the MT.

Theorem C.1. Let $q(z) = \frac{1}{p} \text{Tr}(\mathbf{U} - z\mathbf{I})^{-1}$ and $r(z) = \frac{1}{p} \text{Tr}(\mathbf{W}^T(\mathbf{U} - z\mathbf{I})^{-1}\mathbf{W})$, with $z \in \mathbb{C}$. Then $q(z)$ and $r(z)$ satisfy the following set of equations:

$$\frac{\psi_p v_t^2}{1 + \frac{e^{-2t} \mu_1^2(t) \sigma_x^2 \psi_p}{\psi_n} r + \frac{\psi_p}{\psi_n} v_t^2 q} + \psi_p (s_t^2 - z) + \frac{1 - \psi_p}{q} - \frac{r}{q^2} = 0, \quad (80)$$

$$\frac{e^{-2t} \mu_1^2(t) \sigma_x^2 \psi_p}{1 + \frac{e^{-2t} \mu_1^2(t) \sigma_x^2 \psi_p}{\psi_n} r + \frac{\psi_p}{\psi_n} v_t^2 q} + \Delta_t \mu_1^2 \psi_p + \frac{1}{q} - \frac{1}{r} = 0. \quad (81)$$

The eigenvalue distribution of \mathbf{U} , $\rho(\lambda)$, can then be obtained using the Sokhotski–Plemelj inversion formula $\rho(\lambda) = \lim_{\varepsilon \rightarrow 0^+} \frac{1}{\pi} \text{Im} q(\lambda + i\varepsilon)$.

We first show that the equations of the Stieltjes transform of ρ found in Ref. [9] in the case $\sigma_x = 1$ with linear pencils[3] can be reduced to the equations of Theorem 3.1 with our definitions of μ_1 , s_t and v_t . The equations of [9] read

$$\zeta_1 (s_t^2 - z + e^{-2t} \mu_1^2 \zeta_2 \zeta_3 + v_t^2 \zeta_2 + \Delta_t \mu_1^2 \zeta_4) - 1 = 0 \quad (82)$$

$$\zeta_2 (\psi_n + v_t^2 \psi_p \zeta_1 - e^{-t} \mu_1 \zeta_3) - \psi_n = 0 \quad (83)$$

$$e^{-t} \mu_1 \psi_p \zeta_1 (1 + e^{-t} \mu_1 \zeta_2 \zeta_3) + (1 + (\Delta_t \mu_1^2 \psi_p \zeta_1) \zeta_3) = 0 \quad (84)$$

$$e^{-2t} \mu_1^2 \psi_p \zeta_1 \zeta_2 \zeta_4 + (1 + \Delta_t \mu_1^2 \psi_p \zeta_1) \zeta_4 - 1 = 0, \quad (85)$$

with $\zeta_1 = q$ and $\zeta_{2,3,4}$ auxiliary variables. We make the following change of variables $r = -\frac{\zeta_3}{e^{-t} \mu_1 \psi_p}$. The second equations relates ζ_2 to q and r

$$\zeta_2 = \frac{1}{1 + \frac{e^{-2t} \mu_1^2 \psi_p}{\psi_n} r + \frac{v_t^2 \psi_p}{\psi_n} q}. \quad (86)$$

Injecting this into the second equations gives the second equation of Theorem 3.1. The fourth equation gives

$$\zeta_4 = \frac{1}{1 + \mu_1^2 \psi_p q (\Delta_t + e^{-2t} \zeta_2)}. \quad (87)$$

Injecting this into the first equation gives

$$q (s_t^2 - z + e^{-2t} \mu_1^2 \zeta_2 r (-e^{-t} \mu_1 \psi_p) + v_t^2 \zeta_2 + \Delta_t \mu_1^2 \frac{1}{1 + \mu_1^2 \psi_p q (\Delta_t + e^{-2t} \zeta_2)}) - 1 = 0. \quad (88)$$

After some massaging we find back the first equation of Theorem 3.1.

We now prove Theorem 3.1 using a replica computation, inspired by the calculation done in Ref. [8].

Proof. Our goal is to compute the Stieltjes transform of the matrix \mathbf{U} .

$$q = \lim_{p \rightarrow \infty} \frac{1}{p} \mathbb{E}_{\mathbf{W}, \mathbf{X}, \Omega} [\text{Tr}(\mathbf{U} - z\mathbf{I}_p)^{-1}] \quad (89)$$

$$= -\partial_z \lim_{p \rightarrow \infty} \frac{1}{p} \mathbb{E}_{\mathbf{W}, \mathbf{X}, \Omega} [\log \det(\mathbf{U} - z\mathbf{I}_p)] \quad (90)$$

$$= 2\partial_z \lim_{p \rightarrow \infty} \frac{1}{p} \mathbb{E}_{\mathbf{W}, \mathbf{X}, \Omega} [\log \det(\mathbf{U} - z\mathbf{I}_p)^{-1/2}]. \quad (91)$$

The so-called *replica trick* consists of replacing the $\log x$ by $\lim_{m \rightarrow \infty} \frac{x^m - 1}{m}$. Applying this identity, we obtain

$$q = 2\partial_z \lim_{m \rightarrow \infty} \lim_{p \rightarrow \infty} \frac{1}{pm} \mathbb{E}_{\mathbf{W}, \mathbf{X}, \Omega} [\det(\mathbf{U} - z\mathbf{I}_p)^{-m/2} - 1], \quad (92)$$

where as usual with replica computations we have inverted the order of the limits $p \rightarrow \infty$ and $m \rightarrow 0$. We define the partition function \mathcal{Z} as

$$\mathcal{Z} = \det(\mathbf{U} - z\mathbf{I}_p)^{-1/2} = \int \frac{d\phi}{(2\pi)^{p/2}} e^{-\frac{1}{2}\phi^T(\mathbf{U}-z\mathbf{I}_p)\phi}. \quad (93)$$

We now use the fact that for any integer m

$$\mathbb{E}_{\mathbf{W}, \mathbf{X}, \Omega}[\mathcal{Z}^m] = \int \prod_{a=1}^m \frac{d\phi^a}{(2\pi)^{p/2}} \mathbb{E}_{\mathbf{W}, \mathbf{X}, \Omega}[e^{-\frac{1}{2}\phi^{aT}(\mathbf{U}-z\mathbf{I}_p)\phi^a}] \quad (94)$$

$$= \int \prod_{a=1}^m \frac{d\phi^a}{(2\pi)^{p/2}} e^{-\frac{1}{2}\phi^{aT}(s_t^2-z)\phi^a} \mathbb{E}_{\mathbf{W}, \mathbf{X}, \Omega}[e^{-\frac{1}{2}\phi^{aT}(\frac{\mathbf{G}\mathbf{G}^T}{n} + \Delta_t \mu_1 \frac{\mathbf{W}\mathbf{W}^T}{d})\phi^a}]. \quad (95)$$

We first perform the computation for integer values of m , and then analytically continue the result to the limit $m \rightarrow 0$.

To compute the expectation over \mathbf{X} , \mathbf{W} , and Ω , we need the following standard result from Gaussian integration

$$\int d\mathbf{x} e^{-\frac{1}{2}\mathbf{x}\mathbf{G}\mathbf{x}^T + \mathbf{J}\mathbf{x}^T} = e^{-\frac{1}{2}\det \mathbf{G} + \frac{1}{2}\mathbf{J}\mathbf{G}^{-1}\mathbf{J}^T}, \quad (96)$$

where \mathbf{G} is a square matrix and \mathbf{J} a vector.

Averaging over the data set. The dataset dependence enters through

$$\mathbb{E}_{\mathbf{X}}[e^{-\frac{1}{2}\phi^{aT}(\frac{\mathbf{G}\mathbf{G}^T}{n})\phi^a}] \quad (97)$$

$$= \mathbb{E}_{\mathbf{X}}[e^{-\frac{1}{2n}\phi^{aT}(e^{-t}\mu_1 \frac{\mathbf{W}\mathbf{X}}{\sqrt{d}} + v_t \Omega)(e^{-t}\mu_1 \frac{\mathbf{W}\mathbf{X}}{\sqrt{d}} + v_t \Omega)^T \phi^a}] \quad (98)$$

$$= \mathbb{E}_{\mathbf{X}}[e^{-\frac{e^{-2t}\mu_1^2}{2nd}\phi^{aT}\mathbf{W}\mathbf{X}\mathbf{X}^T\mathbf{W}^T\phi^a} e^{-\frac{e^{-t}\mu_1 v_t}{2\sqrt{dn}}\phi^{aT}(\mathbf{W}\mathbf{X}\Omega^T + \Omega\mathbf{X}^T\mathbf{W}^T)\phi^a} e^{-\frac{v_t^2}{2n}\phi^{aT}\Omega\Omega^T\phi^a}]. \quad (99)$$

We introduce for each replica ϕ^a a Fourier transform of the delta function by using the auxiliary variables $\omega^a, \hat{\omega}^a \in \mathbb{R}^d$ as[†]

$$\int d\omega^a d\hat{\omega}^a e^{i\hat{\omega}^a(\sqrt{p}\omega^a - \phi^{aT}\mathbf{W})} = 1. \quad (100)$$

Hence,

$$\mathbb{E}_{\mathbf{X}}[e^{-\frac{1}{2}\phi^{aT}(\frac{\mathbf{G}\mathbf{G}^T}{n})\phi^a}] \quad (101)$$

$$= \mathbb{E}_{\mathbf{X}}[e^{-\frac{e^{-2t}\mu_1^2}{2nd}\omega^{aT}\mathbf{X}\mathbf{X}^T\omega^a} e^{-\frac{e^{-t}\mu_1\sqrt{p}v_t}{\sqrt{dn}}\sum_{a,\nu}\Omega^\nu\phi^a\omega^a\cdot\mathbf{x}^\nu}] e^{-\frac{v_t^2}{2n}\phi^{aT}\Omega\Omega^T\phi^a}. \quad (102)$$

Denote $\mathbf{G}_{\mathbf{X}} = \frac{e^{-2t}\mu_1^2\sigma_{\mathbf{X}}^2 p}{dn}\sum_a\omega^a\omega^{aT}$ and $(\mathbf{J}_{\mathbf{X}})^\nu_k = \frac{e^{-t}\mu_1\sqrt{p}\sigma_{\mathbf{X}}v_t}{\sqrt{dn}}\sum_a(\Omega^\nu\cdot\phi^a)\omega^a_k$, then

$$\mathbb{E}_{\mathbf{X}}[e^{-\frac{1}{2}\phi^{aT}(\frac{\mathbf{G}\mathbf{G}^T}{n})\phi^a}] = \quad (103)$$

$$e^{-\frac{n}{2}\log\det(\mathbf{I}_d + \mathbf{G}_{\mathbf{X}})} e^{-\frac{e^{-2t}\mu_1^2\sigma_{\mathbf{X}}^2 p v_t^2}{2dn^2}\sum_\nu(\Omega^\nu\cdot\phi^a)(\Omega^\nu\cdot\phi^b)\omega^a_k(1 + \mathbf{G}_{\mathbf{X}})^{-1}_{k,t}\omega^b_t} e^{-\frac{v_t^2}{2n}\phi^{aT}\Omega\Omega^T\phi^a}, \quad (104)$$

where repeated indices mean that there is an implicit summation.

[†]Throughout the computation, we discard non-exponential prefactors, as they give subleading contributions.

Averaging over Ω . The terms that depend on Ω are

$$\mathbb{E}_{\Omega} \left[e^{\frac{e^{-2t} \mu_1^2 p v_i^2 \sigma_{\mathbf{x}}^2}{2dn^2} \sum_{\nu} (\Omega^{\nu} \cdot \phi^a) (\Omega^{\nu} \cdot \phi^b) \omega^a \cdot \omega^b (1 + \mathbf{G}_{\mathbf{x}})_{k,l}^{-1} \omega^b \cdot \omega^l} e^{-\frac{v_i^2}{2n} \phi^{aT} \Omega \Omega^T \phi^a} \right] \quad (105)$$

$$= (\mathbb{E}_{\Omega^{\nu}} \left[e^{\frac{e^{-2t} \mu_1^2 p v_i^2 \sigma_{\mathbf{x}}^2}{2dn^2} \sum_{\nu} (\Omega^{\nu} \cdot \phi^a) (\Omega^{\nu} \cdot \phi^b) \omega^a \cdot \omega^b (1 + \mathbf{G}_{\mathbf{x}})_{k,l}^{-1} \omega^b \cdot \omega^l} e^{-\frac{v_i^2}{2n} \phi^{aT} \Omega^{\nu} \Omega^{\nu T} \phi^a} \right])^n \quad (106)$$

$$= (\mathbb{E}_{\Omega^{\nu}} \left[e^{-\frac{1}{2} \Omega^{\nu T} \phi^a \left(\frac{v_i^2}{n} \delta_{ab} - \frac{e^{-2t} \mu_1^2 p v_i^2 \sigma_{\mathbf{x}}^2}{dn^2} \omega^a \cdot \omega^b (1 + \mathbf{G}_{\mathbf{x}})_{k,l}^{-1} \omega^b \cdot \omega^l \right) \phi^{bT} \Omega^{\nu}} \right])^n \quad (107)$$

$$= e^{-\frac{n}{2} \log \det(1 + \mathbf{G}_{\Omega})}, \quad (108)$$

with

$$(\mathbf{G}_{\Omega})_{k,l} = \phi^a \left(\frac{v_i^2}{n} \delta_{ab} - \frac{e^{-2t} \mu_1^2 p v_i^2 \sigma_{\mathbf{x}}^2}{dn^2} \omega^a \cdot \omega^b (1 + \mathbf{G}_{\mathbf{x}})_{k,l}^{-1} \omega^b \cdot \omega^l \right) \phi^{bT}. \quad (109)$$

We are left with

$$\mathbb{E}_{\mathbf{W}, \mathbf{x}, \Omega} [\mathcal{Z}^m] = \int \prod_{a=1}^m \frac{d\phi^a}{(2\pi)^{p/2}} \int d\omega^a d\hat{\omega}^a \quad (110)$$

$$\mathbb{E}_{\mathbf{W}} \left[e^{-\frac{1}{2} \phi^{aT} (s_i^2 - z) \phi^a} e^{i \hat{\omega}^a (\sqrt{p} \omega^a - \mathbf{W}^T \phi^a)} e^{-\frac{\Delta t \mu_1^2 p}{2d} \omega^a T \omega^a} e^{-\frac{n}{2} \log \det(\mathbf{I}_d + \mathbf{G}_{\mathbf{x}})} e^{-\frac{n}{2} \log \det(\mathbf{I}_d + \mathbf{G}_{\Omega})} \right]. \quad (111)$$

Averaging over the random features \mathbf{W} . \mathbf{W} only appears through $e^{-i \hat{\omega}^a \mathbf{W}^T \phi^a}$.

$$\mathbb{E}_{\mathbf{W}} \left[e^{i \sum_a \hat{\omega}^a (\sqrt{p} \omega^a - \mathbf{W}^T \phi^a)} \right] = e^{i \sqrt{p} \sum_a \hat{\omega}^a \cdot \omega^a} \prod_{i=1}^d (\mathbb{E}_{\mathbf{W}_i \sim \mathcal{N}(0, \mathbf{I}_p)} [e^{-i \sum_a \hat{\omega}_i^a \phi^{aT} W_i}]) \quad (112)$$

$$= e^{i \sqrt{p} \sum_a \hat{\omega}^a \cdot \omega^a} e^{-\frac{1}{2} (\sum_a \hat{\omega}_i^a \phi^a)^2} \quad (113)$$

$$= e^{i \sqrt{p} \sum_a \hat{\omega}^a \cdot \omega^a} e^{-\frac{1}{2} \sum_{a,b} \hat{\omega}^a \cdot \hat{\omega}^b \phi^a \cdot \phi^b}. \quad (114)$$

Averaging over the $\hat{\omega}^a$. We can integrate with respect to $\hat{\omega}$. The only terms that appears with it are

$$\int \prod_a d\hat{\omega}^a e^{i \sqrt{p} \sum_a \hat{\omega}^a \cdot \omega^a} e^{-\frac{1}{2} \sum_{a,b} \hat{\omega}^a \cdot \hat{\omega}^b \phi^a \cdot \phi^b}. \quad (115)$$

Denote $\mathbf{J}_i^a = i \sqrt{p} \omega_i^a$ and $\mathbf{G}_{ij}^{ab} = \delta_{ij} \phi^a \phi^b$, then the integral is of the form

$$\int \prod_a d\hat{\omega}^a e^{\sum_{i,a} \mathbf{J}_i^a \hat{\omega}_i^a} e^{-\frac{1}{2} \sum_{i,j,a,b} \hat{\omega}_i^a \mathbf{G}_{ij}^{ab} \hat{\omega}_j^b} \quad (116)$$

$$= e^{-\frac{1}{2} \log \det(\mathbf{G}) + \frac{1}{2} \mathbf{J}^T \mathbf{G}^{-1} \mathbf{J}}. \quad (117)$$

This gives

$$\mathbb{E}_{\mathbf{W}, \mathbf{x}, \Omega} [\mathcal{Z}^m] = \int \prod_{a=1}^m \frac{d\phi^a}{(2\pi)^{p/2}} \int d\omega^a e^{-\frac{1}{2} \phi^{aT} (s_i^2 - z) \phi^a} e^{-\frac{\Delta t \mu_1^2 p}{2d} \omega^a T \omega^a} \quad (118)$$

$$e^{-\frac{n}{2} \log \det(\mathbf{I}_d + \mathbf{G}_{\mathbf{x}})} e^{-\frac{n}{2} \log \det(\mathbf{I}_d + \mathbf{G}_{\Omega})} e^{-\frac{1}{2} \log \det(\mathbf{G}) + \frac{1}{2} \mathbf{J}^T \mathbf{G}^{-1} \mathbf{J}}. \quad (119)$$

Introducing the order parameters. We define the order parameters as $\mathbf{Q}^{ab} = \frac{1}{p} \phi^a \cdot \phi^b$ and $\mathbf{R}^{ab} = \frac{1}{d} \omega^a \cdot \omega^b$. To enforce these constraints, we use the following delta function representations

$$1 = \int d\mathbf{Q}^{ab} d\hat{\mathbf{Q}}^{ab} e^{\hat{\mathbf{Q}}^{ab} (p\mathbf{Q}^{ab} - \phi^a \cdot \phi^b)}, \quad (120)$$

$$1 = \int d\mathbf{R}^{ab} d\hat{\mathbf{R}}^{ab} e^{\hat{\mathbf{R}}^{ab} (d\mathbf{R}^{ab} - \omega^a \cdot \omega^b)}, \quad (121)$$

and integrate out the Gaussian fields ϕ^a and ω^a to obtain

$$1 = \int d\mathbf{Q}^{ab} d\hat{\mathbf{Q}}^{ab} e^{-\frac{p}{2}(\log \det \hat{\mathbf{Q}} - 2 \text{Tr}(\mathbf{Q}\hat{\mathbf{Q}}))}, \quad (122)$$

$$1 = \int d\mathbf{R}^{ab} d\hat{\mathbf{R}}^{ab} e^{-\frac{d}{2}(\log \det \hat{\mathbf{R}} - 2 \text{Tr}(\mathbf{R}\hat{\mathbf{R}}))}. \quad (123)$$

This allows us to express the replicated partition function $\mathbb{E}_{\mathbf{W}, \mathbf{X}, \Omega}[\mathcal{Z}^m]$ as

$$\mathbb{E}_{\mathbf{W}, \mathbf{X}, \Omega}[\mathcal{Z}^m] = \int d\mathbf{Q} d\hat{\mathbf{Q}} d\mathbf{R} d\hat{\mathbf{R}} e^{-\frac{d}{2} m S(\mathbf{Q}, \hat{\mathbf{Q}}, \mathbf{R}, \hat{\mathbf{R}})}. \quad (124)$$

In the high-dimensional limit, we evaluate the integral via the saddle point method. Taking derivatives with respect to the conjugate order parameters gives

$$\hat{\mathbf{Q}} = -\frac{1}{2} \mathbf{Q}^{-1}, \quad (125)$$

$$\hat{\mathbf{R}} = -\frac{1}{2} \mathbf{R}^{-1}. \quad (126)$$

We can now rewrite the integrand purely in terms of the order parameters \mathbf{Q} and \mathbf{R} . In particular, quadratic terms involving ϕ^a and ω^a simplify to

$$e^{-\frac{1}{2} \phi^{aT} (s_i^2 - z) \phi^a} e^{-\frac{\Delta t \mu_1^2 p}{2d} \omega^{aT} \omega^a} = e^{-\frac{p}{2} (s_i^2 - z) \text{Tr} \mathbf{Q}} e^{-\frac{\Delta t \mu_1^2 p}{2} \text{Tr} \mathbf{R}}. \quad (127)$$

The term $e^{-\frac{p}{2} \omega^T \mathbf{G}^{-1} \omega}$ is rewritten as

$$e^{-\frac{1}{2} \log \det \mathbf{G} - \frac{p}{2} \omega^T \mathbf{G}^{-1} \omega} = e^{-\frac{d}{2} \log \det \mathbf{Q} - \frac{p}{2} d \sum_{ab} \mathbf{R}^{ab} (\mathbf{Q}^{-1})^{ab} \frac{1}{p}} = e^{-\frac{d}{2} \log \det \mathbf{Q} - \frac{d}{2} \text{Tr}(\mathbf{R}\mathbf{Q}^{-1})}. \quad (128)$$

Similarly,

$$e^{-\frac{n}{2} \log \det(\mathbf{I}_d + \mathbf{G}\mathbf{X})} = e^{-\frac{n}{2} \log \det(\mathbf{I}_m + \frac{\mu_1^2 e^{-2t} p \sigma_{\mathbf{x}}^2}{n} \mathbf{R})} \quad (129)$$

The remaining term involves \mathbf{G}_Ω ,

$$e^{-\frac{n}{2} \log \det(\mathbf{I}_d + \mathbf{G}_\Omega)}. \quad (130)$$

Using for instance the Taylor expansion of $(1 + X)^{-1}$, we obtain that

$$\frac{e^{-2t} \mu_1^2 p v_i^2 \sigma_{\mathbf{x}}^2}{dn^2} \omega^a_k (1 + \mathbf{G}\mathbf{X})_{k,l}^{-1} \omega^b_l = \frac{e^{-2t} \mu_1^2 p v_i^2 \sigma_{\mathbf{x}}^2}{n^2} \mathbf{R} (1 + \frac{e^{-2t} \mu_1^2 p v_i^2 \sigma_{\mathbf{x}}^2}{n} \mathbf{R})^{-1}. \quad (131)$$

We also need the fact that, for a matrix $\mathbf{A} \in \mathbb{R}^{p \times p}$, the Hubbard-Stratonovich transform yields

$$\log \det(1 + \frac{1}{n} \phi^a \mathbf{A}^{ab} \phi^{bT}) = \log \det(1 + \frac{p}{n} \mathbf{A}\mathbf{Q}), \quad (132)$$

so that

$$e^{-\frac{n}{2} \log \det(1 + \mathbf{G}_\Omega)} = e^{-\frac{n}{2} \log(1 + \frac{p}{n} (v_i^2 - \frac{e^{-2t} \mu_1^2 p v_i^2 \sigma_{\mathbf{x}}^2}{n} \mathbf{R} (1 + \frac{e^{-2t} \mu_1^2 p \sigma_{\mathbf{x}}^2}{n} \mathbf{R})^{-1}) \mathbf{Q})}. \quad (133)$$

Replica Symmetric Ansatz. We do the following Replica Symmetric (RS) Ansatz for \mathbf{Q} and \mathbf{R} , since in the replica approach to random matrices one does not expect any symmetry breaking (alternatively one could check the stability of the RS solution):

$$\mathbf{Q} = \begin{pmatrix} q & \tilde{q} & \cdots & \tilde{q} \\ \tilde{q} & q & \cdots & \tilde{q} \\ \vdots & \vdots & \ddots & \vdots \\ \tilde{q} & \tilde{q} & \cdots & q \end{pmatrix} \quad (134)$$

$$\mathbf{R} = \begin{pmatrix} r & \tilde{r} & \cdots & \tilde{r} \\ \tilde{r} & r & \cdots & \tilde{r} \\ \vdots & \vdots & \ddots & \vdots \\ \tilde{r} & \tilde{r} & \cdots & r \end{pmatrix}. \quad (135)$$

Under this ansatz, the action reads

$$S = \psi_n \log\left(1 + \frac{p}{n}(v_t^2(q - \tilde{q}) + \mu_1^2 e^{-2t} \sigma_{\mathbf{x}}^2(r - \tilde{r}))\right) + \psi_n \frac{\frac{p}{n}(v_t^2 \tilde{q} + \mu_1^2 e^{-2t} \sigma_{\mathbf{x}}^2 \tilde{r})}{1 + \frac{p}{n}(v_t^2(q - \tilde{q}) + \mu_1^2 e^{-2t} \sigma_{\mathbf{x}}^2(r - \tilde{r}))} \quad (136)$$

$$+ \psi_p(s_t^2 - z)q + \Delta_t \mu_1^2 \psi_p r + \log q + \frac{rq - 2\tilde{q}r + \tilde{r}\tilde{q}}{(q - \tilde{q})^2}. \quad (137)$$

Saddle point equations. The saddle point equations with respect to \tilde{q} and \tilde{r} yield $\tilde{r} = \tilde{q} = 0$. The action therefore simplifies to

$$S(q, r) = \psi_n \log\left(1 + \frac{pv_t^2}{n} \frac{q}{1 + \frac{e^{-2t} \mu_1^2 p \sigma_{\mathbf{x}}^2}{n} r}\right) + \psi_p(s_t^2 - z)q + \Delta_t \mu_1^2 \psi_p r \quad (138)$$

$$+ \psi_n \log\left(1 + \frac{\mu_1^2 e^{-2t} p \sigma_{\mathbf{x}}^2}{n} r\right) + (1 - \psi_p) \log q + \frac{r}{q} - \log r. \quad (139)$$

The saddle point equations are given by

$$\frac{\partial S}{\partial q} = \psi_n \frac{\frac{pv_t^2}{n}}{1 + \frac{e^{-2t} \mu_1^2 p \sigma_{\mathbf{x}}^2}{n} r + \frac{p}{n} v_t^2 q} + \psi_p(s_t^2 - z) + \frac{1 - \psi_p}{q} - \frac{r}{q^2} = 0, \quad (140)$$

$$\frac{\partial S}{\partial r} = \psi_n \frac{\frac{e^{-2t} \mu_1^2 p \sigma_{\mathbf{x}}^2}{n}}{1 + \frac{e^{-2t} \mu_1^2 p \sigma_{\mathbf{x}}^2}{n} r + \frac{p}{n} v_t^2 q} + \Delta_t \mu_1^2 \psi_p + \frac{1}{q} - \frac{1}{r} = 0. \quad (141)$$

Finally, we observe that the solution q^* to the saddle point equations corresponds to the Stieltjes transform of ρ .

$$2\partial_z \frac{1}{p} \frac{\mathbb{E}[\mathcal{Z}^m] - 1}{m} = 2\partial_z \frac{1}{p} \frac{e^{-\frac{d}{2} m S(q^*, r^*)} - 1}{m} \xrightarrow{m \rightarrow 0} -2\partial_z \frac{1}{p} \frac{d}{2} S(q^*, r^*) = q^*. \quad (142)$$

□

C.5 Proof of Theorem 3.2

We recall Theorem 3.2 of the MT.

Theorem C.2 (Informal). Let ρ denote the spectral density of \mathbf{U} .

Regime I: $\psi_p > \psi_n \gg 1$.

$$\rho(\lambda) = \left(1 - \frac{1 + \psi_n}{\psi_p}\right) \delta(\lambda - s_t^2) + \frac{\psi_n}{\psi_p} \rho_1(\lambda) + \frac{1}{\psi_p} \rho_2(\lambda).$$

Regime II: $\psi_n > \psi_p \gg 1$.

$$\rho(\lambda) = \left(1 - \frac{1}{\psi_p}\right) \rho_1(\lambda) + \frac{1}{\psi_p} \rho_2(\lambda).$$

Here, ρ_1 and ρ_2 are atomless measures with disjoint support. The eigenvectors associated with $\delta(\lambda - s_t^2)$ leave both training and test losses unchanged. The support of ρ_1 can be expressed as

$$\left[s_t^2 + v_t^2 \left(1 - \sqrt{\psi_p/\psi_n}\right)^2, s_t^2 + v_t^2 \left(1 + \sqrt{\psi_p/\psi_n}\right)^2 \right],$$

whereas ρ_2 is independent of ψ_n and its support is of order ψ_p .

We now proceed to prove Theorem 3.2.

Proof. Delta peak. We first account for the delta peak in the spectrum. We use the Gaussian equivalence for \mathbf{U} computed in Lemma C.1. Let $\boldsymbol{\Omega}^\nu \in \mathbb{R}^p$ be the ν th column of $\boldsymbol{\Omega}$ and $\mathbf{W}_i \in \mathbb{R}^p$ the i th row of \mathbf{W} . Suppose a vector $\mathbf{v} \in \mathbb{R}^p$ lies in the kernel of all these

$$\forall \nu = 1, \dots, n, \quad \sum_{k=1}^p \boldsymbol{\Omega}_k^\nu \mathbf{v}_k = 0, \quad (143)$$

$$\forall k = 1, \dots, d, \quad \sum_{i=1}^p \mathbf{W}_{ik} \mathbf{v}_k = 0. \quad (144)$$

then $\mathbf{U}\mathbf{v} = s_t^2 \mathbf{v}$. These are $n + d$ linear constraints on a vector of size p hence there are non trivial solutions for $n + d \leq p$. Hence a delta-peak at s_t^2 appears as soon as $\psi_p \geq \psi_n + 1$. Next, we extract its weight. Recall that the Stieltjes transform satisfies

$$q(z) = \int \frac{\rho(\lambda)}{\lambda - z} d\lambda,$$

and a point mass of weight f at $\lambda = s_t^2$ contributes $\frac{-f}{z - s_t^2} \approx \frac{f}{\varepsilon}$ as $z \rightarrow s_t^2 - \varepsilon$. Meanwhile

$$r(z) = \frac{1}{p} \text{Tr}[\mathbf{W}^T (\mathbf{U} - z\mathbf{I})^{-1} \mathbf{W}]$$

remains finite in that limit, since the corresponding eigenvectors satisfy $\mathbf{W}\mathbf{v} = 0$. We substitute this Ansatz into the equations of Theorem 3.1. The first equation reads

$$\psi_n \frac{\frac{pv_t^2}{n}}{1 + \frac{e^{-2t} \mu_1^2 p \sigma_x^2}{n} r + \frac{p}{n} v_t^2 q} + \psi_p (s_t^2 - z) + \frac{1 - \psi_p}{q} - \frac{r}{q^2} = 0, \quad (145)$$

and simplifies to

$$\frac{\psi_n \varepsilon}{f} + \psi_p \varepsilon + \frac{(1 - \psi_p) \varepsilon}{f} = 0. \quad (146)$$

It readily gives

$$f = 1 - \frac{1}{\psi_p} - \frac{\psi_n}{\psi_p}. \quad (147)$$

Thus the point mass at s_t^2 has weight $1 - \frac{1}{\psi_p} - \frac{\psi_n}{\psi_p}$, in agreement with the constraints-degrees of freedom analysis presented above.

Finally, one checks that these isolated eigenvalues do not contribute to the train and test losses. After expanding the square they read

$$\mathcal{L}_{\text{train}}(\mathbf{A}) = 1 + \frac{\Delta_t}{d} \text{Tr}\left(\frac{\mathbf{A}^T}{\sqrt{p}} \frac{\mathbf{A}}{\sqrt{p}} \mathbf{U}\right) + \frac{2\sqrt{\Delta_t}}{d} \text{Tr}\left(\frac{\mathbf{A}}{\sqrt{p}} \mathbf{V}\right) \quad (148)$$

$$\mathcal{L}_{\text{test}}(\mathbf{A}) = 1 + \frac{\Delta_t}{d} \text{Tr}\left(\frac{\mathbf{A}^T}{\sqrt{p}} \frac{\mathbf{A}}{\sqrt{p}} \tilde{\mathbf{U}}\right) + \frac{2\sqrt{\Delta_t}}{d} \text{Tr}\left(\frac{\mathbf{A}}{\sqrt{p}} \tilde{\mathbf{V}}\right) \quad (149)$$

The terms that appear in the loss are of the form $\text{Tr}(\mathbf{A}^T \mathbf{A} \dots)$ and $\text{Tr}(\mathbf{A} \mathbf{W})$. The trace can be decomposed on the basis of eigenvectors of \mathbf{U} . The eigenvectors associated with the delta peak satisfy $\mathbf{W}^T \mathbf{v} = 0$. Looking at the expression of the matrix $\mathbf{A} = \mathbf{W}^T \dots + \mathbf{A}_0$, one can easily see that if $\mathbf{A}_0 = 0$ (we indeed consider initial conditions equal to zero) then $\mathbf{v}^T \mathbf{A}^T = 0$ and the subspace corresponding to these isolated eigenvalues does not contribute to the loss.

First bulk. Using the expression for $q = \frac{1}{p} \text{Tr} \frac{1}{\mathbf{U} - z\mathbf{I}_p}$ and $r = \frac{1}{p} \text{Tr} \mathbf{W}^T \frac{1}{\mathbf{U} - z\mathbf{I}_p} \mathbf{W}$ we make the following Ansatz in the large ψ_p limit:

$$q = \mathcal{O}_{\psi_p}(1), \quad r = \mathcal{O}_{\psi_p}\left(\frac{1}{\psi_p}\right). \quad (150)$$

In this limit the first saddle point equation becomes

$$\frac{v_t^2}{1 + \frac{p}{n}v_t^2 q} + s_t^2 - z - \frac{1}{q} = 0. \quad (151)$$

This is a quadratic polynomial in q . If its discriminant is negative then the solutions are imaginary and thus the density of eigenvalues is non-zero. The edge of the bulk are where the discriminant vanishes

$$\Delta = (s_t^2 - \lambda(1 - \frac{p}{n})v_t^2)^2 + 4(s_t^2 - \lambda)\frac{p}{n}v_t^2 = 0. \quad (152)$$

It vanishes for

$$\lambda_{\pm} = s_t^2 + v_t^2 \left(1 \pm \sqrt{\frac{p}{n}} \right)^2 \quad (153)$$

which are the edges of the first bulk ρ_1 . We have checked this result, and hence validated the Ansatz solving numerically the equations on r, q .

Second bulk. To analyze the second band of eigenvalues, we scale $q = \frac{\hat{q}}{\psi_p}$, $r = \frac{\hat{r}}{\psi_p}$ as in the Marchenko–Pastur law [28]. At leading order, the saddle point equations become (neglecting $\mathcal{O}(1/\psi_n)$ terms)

$$(v_t^2 + s_t^2 - z) - \frac{1 - \psi_p}{\hat{q}} - \frac{\hat{r}}{\hat{q}^2} = 0 \quad (154)$$

$$\mu_1^2(\sigma_x^2 e^{-2t} + \Delta_t) + \frac{1}{\hat{q}} - \frac{1}{\hat{r}} = 0. \quad (155)$$

We use $v_t^2 + s_t^2 = \mu_*^2$, $\sigma_x^2 e^{-2t} + \Delta_t = \Gamma_t^2$ and replace \hat{r} in the first equation

$$(\mu_*^2 - z) - \frac{1 - \psi_p}{\hat{q}} - \frac{1}{\hat{q}(1 + \mu_1^2 \Gamma_t^2 \hat{q})} = 0. \quad (156)$$

This is the equation of the Stieltjes of a Marchenko–Pastur distribution (see [28] for a proof) whose edges are

$$\lambda_{\pm}^{MP} = \mu_*^2 + \mu_1^2 \Gamma_t^2 (1 \pm \sqrt{\psi_p})^2, \quad (157)$$

which scales as $\mathcal{O}(\psi_p)$. Furthermore, the weight of the bulk in the Marchenko–Pastur distribution is $1/\psi_p$. It enables us to deduce the weight of the first bulk of ρ since we know the weight of the delta peak. Again, we have checked these results, and hence validated the Ansatz solving numerically the equations on r, q . \square

C.6 Dynamic on the fast timescales

In the following we denote for a matrix $\mathbf{A} \in \mathbb{R}^{p \times p}$,

$$\|\mathbf{A}\|_{\text{op}} = \sup_{\mathbf{v} \in \mathbb{R}^p, \|\mathbf{v}\|=1} \|\mathbf{A}\mathbf{v}\| \quad (158)$$

the operator norm and

$$\|\mathbf{A}\|_{\text{F}} = \left(\sum_{i,j=1}^p \mathbf{A}_{ij}^2 \right)^{1/2} \quad (159)$$

the Frobenius norm. Before deriving the fast-time behavior, we need the following lemma.

Lemma C.4. *The operator norm of $\mathbf{U} - \tilde{\mathbf{U}}$ satisfies*

$$\|(\mathbf{U} - \tilde{\mathbf{U}})\|_{\text{op}} = \mathcal{O}\left(\frac{\psi_p}{\sqrt{\psi_n}}\right) \quad (160)$$

when $p \gg n \gg d$.

Proof. We take $\sigma_x = 1$ but the proof can be done for arbitrary variance. Without loss of generality, we consider eigenvectors \mathbf{v} of \mathbf{U} with unit norm. We first write that

$$\mathbf{U} - \tilde{\mathbf{U}} = \mu_1^2 e^{-2t} \frac{\mathbf{W}}{\sqrt{d}} \left(\frac{\mathbf{X}\mathbf{X}^T}{n} - \mathbf{I}_d \right) \frac{\mathbf{W}^T}{\sqrt{d}} + v_t^2 \left(\frac{\boldsymbol{\Omega}\boldsymbol{\Omega}^T}{n} - \mathbf{I}_p \right) + \frac{\mu_1 v_t e^{-t}}{n\sqrt{d}} (\boldsymbol{\Omega}\mathbf{X}^T \mathbf{W}^T + \mathbf{W}\mathbf{X}\boldsymbol{\Omega}^T). \quad (161)$$

We can bound its operator norm

$$\begin{aligned} \|(\mathbf{U} - \tilde{\mathbf{U}})\|_{\text{op}} &\leq C_1 \left\| \frac{\mathbf{W}}{\sqrt{d}} \left(\frac{\mathbf{X}\mathbf{X}^T}{n} - \mathbf{I}_d \right) \frac{\mathbf{W}^T}{\sqrt{d}} \right\|_{\text{op}} + C_2 \left\| \left(\frac{\boldsymbol{\Omega}\boldsymbol{\Omega}^T}{n} - \mathbf{I}_p \right) \right\|_{\text{op}} \\ &\quad + \frac{C_3}{n\sqrt{d}} \|\boldsymbol{\Omega}\mathbf{X}^T \mathbf{W}^T + \mathbf{W}\mathbf{X}\boldsymbol{\Omega}^T\|_{\text{op}}, \end{aligned} \quad (162)$$

where C_1, C_2, C_3 are constants independent of p, n, d . We bound each of the three terms of the right hand side. We use the fact that for a symmetric matrix the operator norm $\|\cdot\|_{\text{op}}$ is equal to its largest eigenvalue.

First Term. We observe that $\frac{\mathbf{W}}{\sqrt{d}} \left(\frac{\mathbf{X}\mathbf{X}^T}{n} - \mathbf{I}_d \right) \frac{\mathbf{W}^T}{\sqrt{d}}$ and $\frac{\mathbf{W}^T}{\sqrt{d}} \frac{\mathbf{W}}{\sqrt{d}} \left(\frac{\mathbf{X}\mathbf{X}^T}{n} - \mathbf{I}_d \right)$ have the same eigenvalues up to the multiplicity of 0[†]. We then use the sub-multiplicativity of the operator norm

$$\left\| \frac{\mathbf{W}}{\sqrt{d}} \left(\frac{\mathbf{X}\mathbf{X}^T}{n} - \mathbf{I}_d \right) \frac{\mathbf{W}^T}{\sqrt{d}} \right\|_{\text{op}} \leq \left\| \frac{\mathbf{W}^T}{\sqrt{d}} \frac{\mathbf{W}}{\sqrt{d}} \right\|_{\text{op}} \left\| \left(\frac{\mathbf{X}\mathbf{X}^T}{n} - \mathbf{I}_d \right) \right\|_{\text{op}}. \quad (163)$$

The spectrum of $\left(\frac{\mathbf{X}\mathbf{X}^T}{n} - \mathbf{I}_d \right)$ is the Marchenko-Pastur law whose largest eigenvalue is of order $\sqrt{d/n}$ while for $\frac{\mathbf{W}^T \mathbf{W}}{d}$ it is order $\frac{p}{d}$. The bound reads

$$\left\| \frac{\mathbf{W}}{\sqrt{d}} \left(\frac{\mathbf{X}\mathbf{X}^T}{n} - \mathbf{I}_d \right) \frac{\mathbf{W}^T}{\sqrt{d}} \right\|_{\text{op}} \leq \mathcal{O}\left(\frac{p}{\sqrt{nd}}\right) \quad (164)$$

Second term.

$$\left\| \left(\frac{\boldsymbol{\Omega}\boldsymbol{\Omega}^T}{n} - \mathbf{I}_p \right) \right\|_{\text{op}}. \quad (165)$$

We observe that the spectrum of $\boldsymbol{\Omega}\boldsymbol{\Omega}^T/n - \mathbf{I}_p$ is Marchenko-Pastur and thus its largest eigenvalue is order $\mathcal{O}(p/n)$ yielding

$$\left\| \left(\frac{\boldsymbol{\Omega}\boldsymbol{\Omega}^T}{n} - \mathbf{I}_p \right) \right\|_{\text{op}} \leq \mathcal{O}(p/n) \quad (166)$$

Third term.

$$\|\boldsymbol{\Omega}\mathbf{X}^T \mathbf{W}^T + \mathbf{W}\mathbf{X}\boldsymbol{\Omega}^T\|_{\text{op}}. \quad (167)$$

We first bound the operator norm by the Frobenius norm.

$$\|\boldsymbol{\Omega}\mathbf{X}^T \mathbf{W}^T + \mathbf{W}\mathbf{X}\boldsymbol{\Omega}^T\|_{\text{op}} \leq 2\|\boldsymbol{\Omega}\mathbf{X}^T \mathbf{W}^T\|_{\text{F}}. \quad (168)$$

We expand the square

$$\|\boldsymbol{\Omega}\mathbf{X}^T \mathbf{W}^T + \mathbf{W}\mathbf{X}\boldsymbol{\Omega}^T\|_{\text{F}}^2 = C \sum_{k=1}^d \sum_{i=1}^p \left(\sum_{\nu=1}^n \Omega_i^\nu \mathbf{X}_k^\nu \mathbf{W}_{kl} \right)^2. \quad (169)$$

The Central Limit Theorem yields

$$\sum_{\nu=1}^n \Omega_i^\nu \mathbf{X}_k^\nu \mathbf{W}_{kl} = \mathcal{O}(\sqrt{n}) \mathbf{W}_{kl}, \quad (170)$$

[†]They both have the same moments $\text{Tr}(\cdot)^k$ owing to the cyclicity of the trace.

hence

$$\frac{1}{n\sqrt{d}} \|\Omega \mathbf{X}^T \mathbf{W}^T + \mathbf{W} \mathbf{X} \Omega^T\|_{\text{op}} = \mathcal{O}\left(\frac{\sqrt{ndp}}{n\sqrt{d}}\right) = \mathcal{O}\left(\sqrt{\frac{p}{n}}\right) \quad (171)$$

Putting all the contributions together yields

$$\|(\mathbf{U} - \tilde{\mathbf{U}})\|_{\text{op}} \leq \mathcal{O}\left(\frac{p}{\sqrt{dn}}\right). \quad (172)$$

□

Proposition C.2 (Informal). *On timescales $1 \ll \tau \ll \psi_n$, both the train and test losses satisfy*

$$\mathcal{L}_{\text{train}} \simeq \mathcal{L}_{\text{test}} \simeq 1 - \mathcal{O}(\Delta_t). \quad (173)$$

Proof. According to the spectral analysis of \mathbf{U} done previously, there are two bulks in the spectrum that contribute to the dynamic: a first bulk with eigenvalues of order $\frac{\psi_p}{\psi_n}$ and a second bulk with eigenvalues of order ψ_p in the $\psi_p, \psi_n \gg 1$ limit. Hence in the regime $1 \ll \tau \ll \psi_n$, $e^{-\lambda \frac{\Delta_t \tau}{\psi_p}} \sim 0$ if λ is in the second bulk and is $e^{-\lambda \frac{\Delta_t \tau}{\psi_p}} \sim 1$ if λ is in the first bulk. We remind the expressions of the train and test loss

$$\mathcal{L}_{\text{train}}(\mathbf{A}) = 1 + \frac{\Delta_t}{d} \text{Tr}\left(\frac{\mathbf{A}^T}{\sqrt{p}} \frac{\mathbf{A}}{\sqrt{p}} \mathbf{U}\right) + \frac{2\sqrt{\Delta_t}}{d} \text{Tr}\left(\frac{\mathbf{A}}{\sqrt{p}} \mathbf{V}\right) \quad (174)$$

$$\mathcal{L}_{\text{test}}(\mathbf{A}) = 1 + \frac{\Delta_t}{d} \text{Tr}\left(\frac{\mathbf{A}^T}{\sqrt{p}} \frac{\mathbf{A}}{\sqrt{p}} \tilde{\mathbf{U}}\right) + \frac{2\sqrt{\Delta_t}}{d} \text{Tr}\left(\frac{\mathbf{A}}{\sqrt{p}} \tilde{\mathbf{V}}\right) \quad (175)$$

and use the expression of $\mathbf{A}(\tau)$ in Proposition C.1 that we expand on the basis of eigenvectors $\{\mathbf{v}_\lambda\}_{\lambda=1}^p$ of \mathbf{U} .

$$\frac{\mathbf{A}(\tau)}{\sqrt{p}} = \frac{1}{\sqrt{\Delta_t}} \mathbf{V}^T \mathbf{U}^{-1} (e^{-\frac{2\Delta_t}{d} \mathbf{U} \tau} - \mathbf{I}_p) \quad (176)$$

$$= \frac{1}{\sqrt{\Delta_t}} \mathbf{V}^T \mathbf{U}^{-1} \sum_{\lambda} (e^{-\frac{2\Delta_t}{d} \lambda \tau} - 1) \mathbf{v}_\lambda \mathbf{v}_\lambda^T \quad (177)$$

$$\sim -\frac{1}{\sqrt{\Delta_t}} \mathbf{V}^T \mathbf{U}^{-1} \sum_{\lambda \in \rho_2} \mathbf{v}_\lambda \mathbf{v}_\lambda^T, \quad (178)$$

where $\lambda \in \rho_2$ means that the eigenvalue λ belongs to the second bulk. We also have that \mathbf{V} and $\tilde{\mathbf{V}}$ have the same GEP and they thus cancel each other when computing the generalization loss $\mathcal{L}_{\text{gen}} = \mathcal{L}_{\text{test}} - \mathcal{L}_{\text{train}}$. It reads

$$\mathcal{L}_{\text{gen}} = -\frac{\mu_1^2 \Delta_t}{d} \text{Tr}\left(\sum_{\lambda, \lambda' \in \rho_2} \mathbf{v}_{\lambda'} \mathbf{v}_{\lambda'}^T \mathbf{U}^{-1} \frac{\mathbf{W} \mathbf{W}^T}{d} \mathbf{U}^{-1} \mathbf{v}_\lambda \mathbf{v}_\lambda^T (\mathbf{U} - \tilde{\mathbf{U}})\right) \quad (179)$$

$$= -\frac{\mu_1^2 \Delta_t}{d} \left(\sum_{\lambda, \lambda' \in \rho_2} \mathbf{v}_{\lambda'}^T \mathbf{U}^{-1} \frac{\mathbf{W} \mathbf{W}^T}{d} \mathbf{U}^{-1} \mathbf{v}_\lambda \mathbf{v}_\lambda^T (\mathbf{U} - \tilde{\mathbf{U}}) \mathbf{v}_{\lambda'}\right) \quad (180)$$

$$= -\frac{\mu_1^2 \Delta_t}{d} \left(\sum_{\lambda, \lambda' \in \rho_2} \mathbf{v}_{\lambda'}^T \frac{1}{\lambda'} \frac{\mathbf{W} \mathbf{W}^T}{d} \frac{1}{\lambda} \mathbf{v}_\lambda \mathbf{v}_\lambda^T (\mathbf{U} - \tilde{\mathbf{U}}) \mathbf{v}_{\lambda'}\right) \quad (181)$$

$$\begin{aligned} &= \frac{\Delta_t}{d} \sum_{\lambda, \lambda' \in \rho_2} \mathbf{v}_{\lambda'}^T \frac{1}{\lambda'} (\mathbf{U} - \tilde{\mathbf{U}}) \frac{1}{\lambda} \mathbf{v}_\lambda \mathbf{v}_\lambda^T (\mathbf{U} - \tilde{\mathbf{U}}) \mathbf{v}_{\lambda'} + \frac{\mu_*^2 \Delta_t}{d} \sum_{\lambda \in \rho_2} \frac{1}{\lambda^2} \mathbf{v}_\lambda^T (\mathbf{U} - \tilde{\mathbf{U}}) \mathbf{v}_\lambda \\ &\quad - \frac{\Delta_t}{d} \sum_{\lambda, \lambda' \in \rho_2} \mathbf{v}_{\lambda'}^T \frac{1}{\lambda'} \mathbf{U} \frac{1}{\lambda} \mathbf{v}_\lambda \mathbf{v}_\lambda^T (\mathbf{U} - \tilde{\mathbf{U}}) \mathbf{v}_{\lambda'}, \end{aligned} \quad (182)$$

where to go from (181) to (182) we replaced $\mu_1^2 \frac{\mathbf{W} \mathbf{W}^T}{d}$ by $\tilde{\mathbf{U}} - \mu_*^2 \mathbf{I}_p$. We then use Lemma C.4 — which tells that the operator norm of $\mathbf{U} - \tilde{\mathbf{U}}$ in the subspace spanned by the eigenvectors of the second bulk is

bounded by $\mathcal{O}(\frac{p}{\sqrt{dn}})$ — enables to bound the three terms. First

$$|\frac{\mu_*^2 \Delta_t}{d} \sum_{\lambda \in \rho_2} \frac{1}{\lambda^2} \mathbf{v}_\lambda^T (\mathbf{U} - \tilde{\mathbf{U}}) \mathbf{v}_\lambda| \leq \mathcal{O}(\frac{1}{\psi_p^2} \frac{\psi_p}{\sqrt{\psi_n}}) = \mathcal{O}(\frac{1}{\psi_p \sqrt{\psi_n}}), \quad (183)$$

where we used that the eigenvalues in the second bulk are order ψ_p and that the sum is composed of d terms. Second,

$$|\frac{\Delta_t}{d} \sum_{\lambda, \lambda' \in \rho_2} \mathbf{v}_{\lambda'}^T \frac{1}{\lambda'} \mathbf{U} \frac{1}{\lambda} \mathbf{v}_\lambda \mathbf{v}_{\lambda'}^T (\mathbf{U} - \tilde{\mathbf{U}}) \mathbf{v}_{\lambda'}| = |\frac{\Delta_t}{d} \sum_{\lambda \in \rho_2} \frac{1}{\lambda} \mathbf{v}_\lambda^T (\mathbf{U} - \tilde{\mathbf{U}}) \mathbf{v}_\lambda| \leq \mathcal{O}(\frac{1}{\psi_p} \frac{\psi_p}{\sqrt{\psi_n}}) \quad (184)$$

$$\leq \mathcal{O}(\frac{1}{\sqrt{\psi_n}}). \quad (185)$$

Finally

$$|\frac{\Delta_t}{d} \sum_{\lambda, \lambda' \in \rho_2} \mathbf{v}_{\lambda'}^T \frac{1}{\lambda'} (\mathbf{U} - \tilde{\mathbf{U}}) \frac{1}{\lambda} \mathbf{v}_\lambda \mathbf{v}_{\lambda'}^T (\mathbf{U} - \tilde{\mathbf{U}}) \mathbf{v}_{\lambda'}| \leq \mathcal{O}(\frac{1}{\psi_p^2} \frac{\psi_p^2}{\psi_n}) = \mathcal{O}(\frac{1}{\psi_n}). \quad (186)$$

The three bounds yield that \mathcal{L}_{gen} vanishes asymptotically in the large number of data and large number of parameters regime. Therefore, on the fast timescale we find $\mathcal{L}_{\text{train}} \simeq \mathcal{L}_{\text{test}}$. Let us now focus on $\mathcal{L}_{\text{train}}$

$$\mathcal{L}_{\text{train}} = 1 + \frac{\mu_1^2 \Delta_t}{d} \left(\sum_{\lambda, \lambda' \in \rho_2} \mathbf{v}_{\lambda'}^T \frac{1}{\lambda'} \frac{\mathbf{W}\mathbf{W}^T}{d} \frac{1}{\lambda} \mathbf{v}_\lambda \mathbf{v}_{\lambda'}^T \mathbf{U} \mathbf{v}_{\lambda'} \right) - \frac{2\Delta_t \mu_1^2}{d} \sum_{\lambda \in \rho_2} \mathbf{v}_\lambda^T \frac{\mathbf{W}\mathbf{W}^T}{d} \mathbf{U}^{-1} \mathbf{v}_\lambda \quad (187)$$

$$= 1 - \frac{\mu_1^2 \Delta_t}{d} \sum_{\lambda \in \rho_2} \frac{1}{\lambda} \mathbf{v}_\lambda^T \frac{\mathbf{W}\mathbf{W}^T}{d} \mathbf{v}_\lambda. \quad (188)$$

There are d values in the sum and the eigenvalues of \mathbf{U} and $\frac{\mathbf{W}\mathbf{W}^T}{d}$ are both order $\mathcal{O}(\psi_p)$ hence the sum divided by d is a positive $\mathcal{O}(1)$ quantity thus in this training time regime, $1 \ll \tau \ll \psi_n$, we obtain:

$$\mathcal{L}_{\text{train}} \sim \mathcal{L}_{\text{test}} = 1 - \mathcal{O}(\Delta_t). \quad (189)$$

□

D Numerical experiments for Random Features

Details on the numerical experiments. All the numerical experiments for the RFNN were conducted using $\sigma = \tanh$ and $\sigma_x = 1$ unless specified. At each step, the gradient of the loss was computed using the full batch of data points. The train loss was estimated by adding noise to each data point $N = 100$ times. The test loss was computed by drawing n new points from the data distribution and noising each one N times. The error on the score was evaluated by drawing 10,000 points from the noisy distribution $P_t = \mathcal{N}(0, \Gamma_t^2 \mathbf{I}_d)$.

Effect of t . We present plots for different diffusion times t in Fig. 12 and show that the rescaling of the training times τ by $\tau_{\text{mem}} = \psi_p / \Delta_t \lambda_{\text{min}}$ also makes the loss curves collapse. Of particular interest is the behavior of τ_{mem} , and more specifically the ratio $\tau_{\text{mem}} / \tau_{\text{gen}}$, at small t . Recall that

$$\lambda_{\text{min}} = s_t^2 + v_t^2 \left(1 - \sqrt{\frac{\psi_p}{\psi_n}} \right)^2.$$

In the overparameterized regime $p \gg n$, this ratio is independent of t since $v_t^2 \sim \mu_*^2$ and $s_t^2 \sim t$. However, when $p \sim n$, a nontrivial scaling emerges: since $\lambda_{\text{min}} \sim s_t^2 \sim t$, it follows that

$$\frac{\tau_{\text{mem}}}{\tau_{\text{gen}}} \sim \frac{1}{t},$$

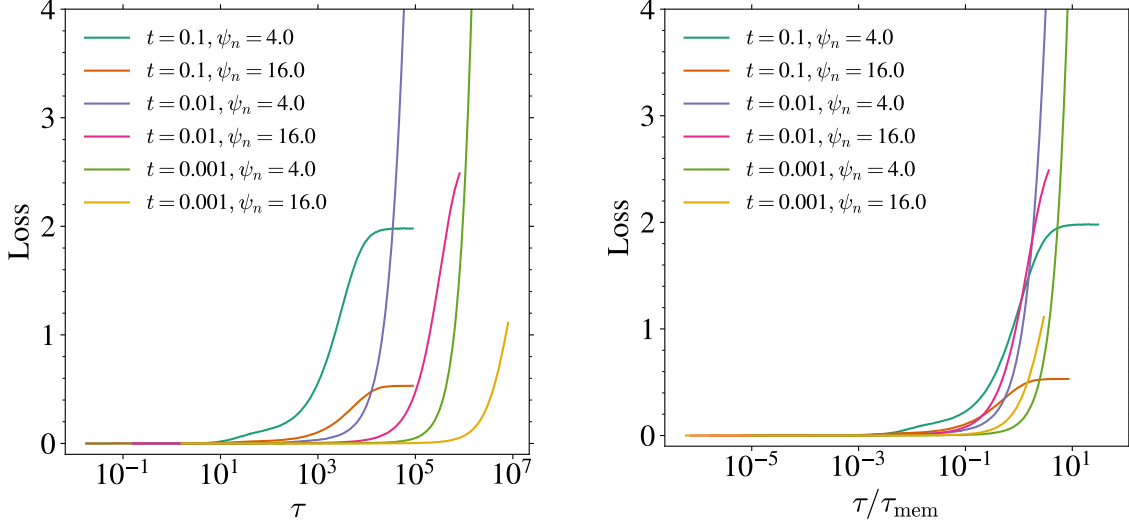


Figure 12: Generalization loss for different diffusion times t . Generalization loss \mathcal{L}_{gen} against (Left) training time τ and (Right) rescaled training time τ/τ_{gen} for different $\psi_p = 32$, $d = 100$ and different ψ_n and t .

implying that the two timescales become increasingly separated. It is unclear whether this behavior is related to specific properties of the learned score function, and is related to the approach of the interpolation threshold. We leave this question for future investigation.

Experiments with $\sigma_x^2 \neq 1$. In Fig. 13, we present train and test loss curves for $\sigma_x \neq 1$. We see that our prediction of the timescale of memorization computed in the MT holds for general data variance.

Scaling of $\mathcal{E}_{\text{score}}$ with n . In the RF model, the error with respect to the true score, as defined in the main text,

$$\mathcal{E}_{\text{Score}} = \frac{1}{d} \mathbb{E}_{\mathbf{y} \sim \mathcal{N}(0, \Gamma_t^2 I_p)} \left[\left\| \mathbf{s}_{\mathbf{A}(\tau)}(\mathbf{y}) + \frac{\mathbf{y}}{\Gamma_t^2} \right\|^2 \right], \quad (190)$$

serves as a measure of the generalization capability of the generative process. As shown in [42], the Kullback–Leibler divergence between the true data distribution $P_{\mathbf{x}}$ and the generated distribution \hat{P} can be upper bounded

$$\mathcal{D}_{\text{KL}}(P_{\mathbf{x}} \parallel \hat{P}) \leq \frac{d}{2} \int dt \mathcal{E}_{\text{Score}}(\mathbf{A}_t), \quad (191)$$

where the integral is taken over all estimations of the parameter matrix \mathbf{A} at all diffusion times t . This bound assumes that the reverse dynamics are integrated exactly, starting from infinite time. In practical settings, however, one typically relies on an approximate scheme and initiates the reverse process at a large but finite time T . A generalization of this bound under such conditions can be found in [4]. We have numerically investigate the behaviour of $\mathcal{E}_{\text{score}}$ on Fig. 14. On the fast timescale τ_{gen} , it decreases until a minimal value $\mathcal{E}_{\text{score}}^*$ that depends only on ψ_n with a power-law $\psi_n^{-\eta}$ with $\eta \simeq 0.59$. We leave for future work performing an accurate numerical estimate of η and a developing a theory for it.

Spectrum of \mathbf{U} . In Fig. 15, we compare the solutions of the equations of Theorem 3.1 to the histogram of finite size realizations of \mathbf{U} .

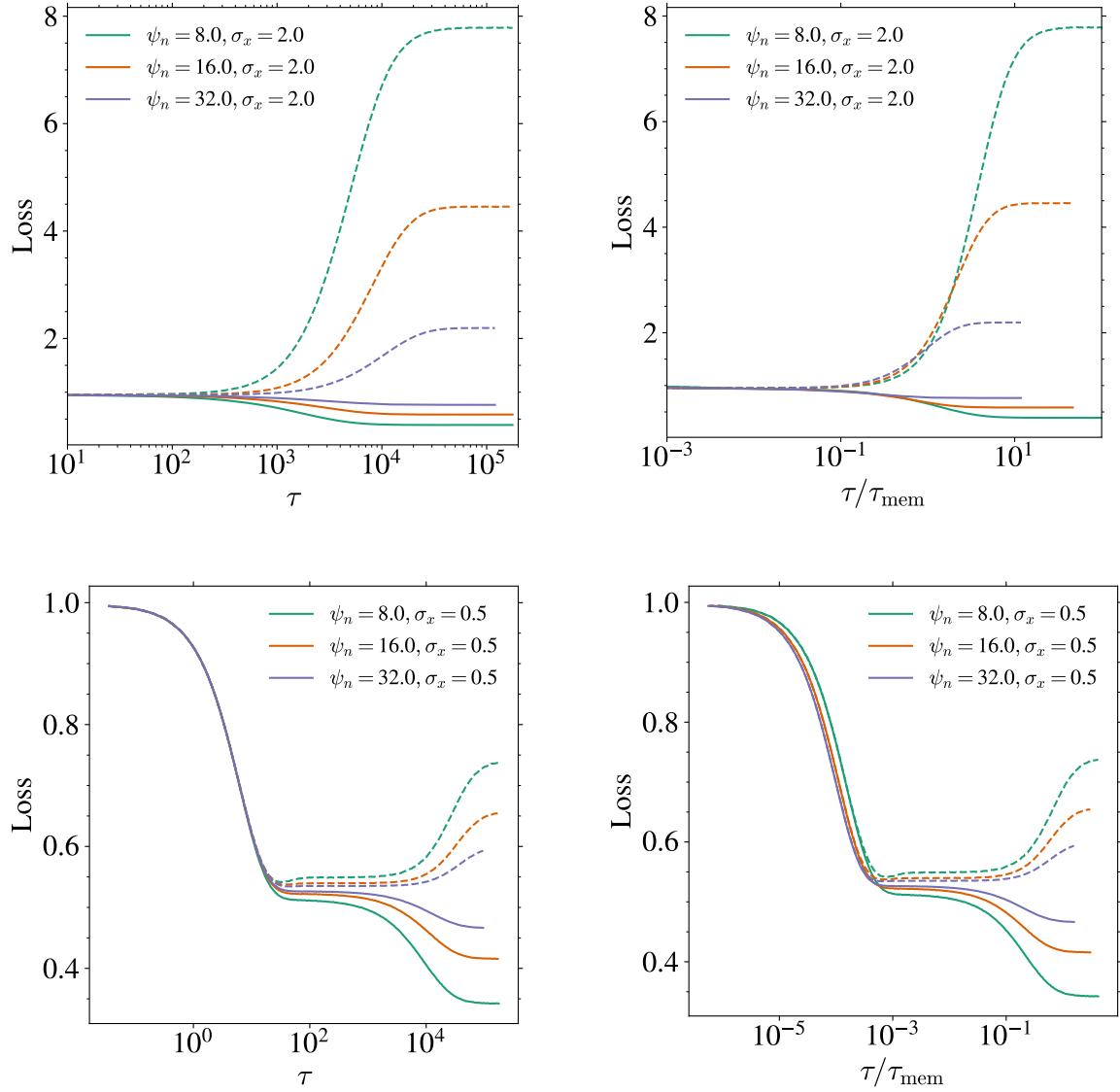


Figure 13: Different σ_x^2 . Train loss (solid line) and test loss (dotted line) for \mathcal{L}_{gen} for $\psi_p = 64, t = 0.1, d = 100$, different ψ_n and $\sigma_x = 2.0$ (top) and $\sigma_x = 0.5$ (bottom) against the training time τ and the rescaled training time τ/τ_{mem} .

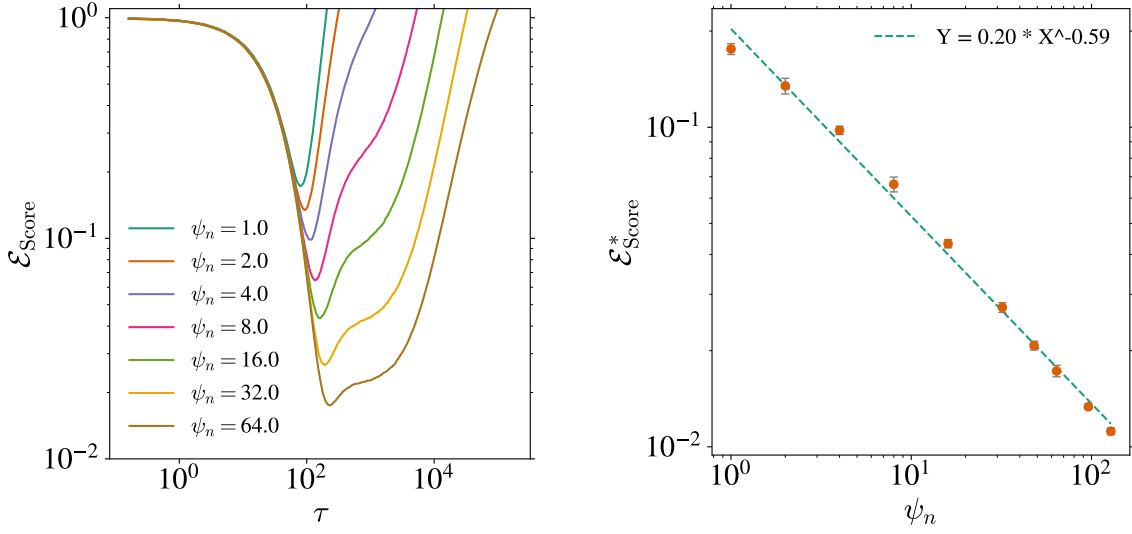


Figure 14: Effect of ψ_n on $\mathcal{E}_{\text{Score}}^*$. (Left) Error between the learned score and the true score $\mathcal{E}_{\text{Score}}$ for $\psi_p = 32$, $t = 0.01$, and various values of ψ_n . (Right) Minimum score error $\mathcal{E}_{\text{Score}}^* = \min_{\tau}[\mathcal{E}_{\text{Score}}(\tau)]$ as a function of ψ_n , showing a power-law decay with exponent approximately -0.59 . The error bars correspond to thrice the standard deviation over 10 runs with new initial conditions.

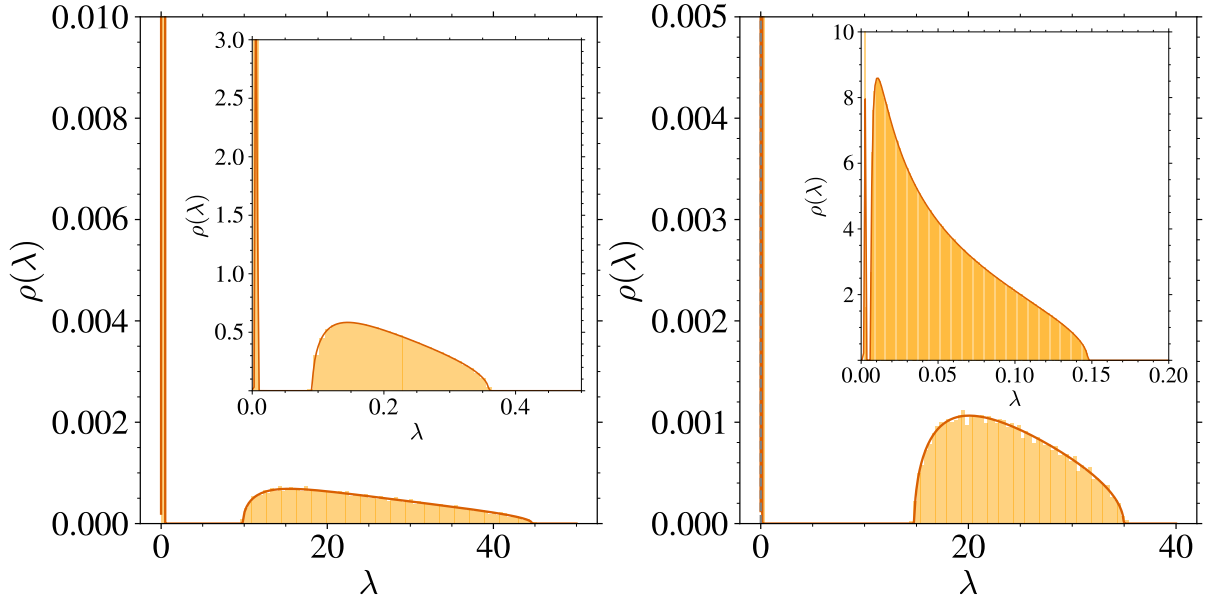


Figure 15: Spectrum of U. Solutions of the equations in Theorem 3.1. (solid lines) and empirical spectrum for $d = 100$ (histogram). (Left) $\psi_p = 64, \psi_n = 8, t = 0.01$. (Right) $\psi_p = 64, \psi_n = 32, t = 0.01$.